

## B335: A LABORATORY FOR ASTROCHEMISTRY IN A COLLAPSING CLOUD

NEAL J. EVANS II

Department of Astronomy, The University of Texas at Austin, 1 University Station C1400, Austin, Texas  
78712-0259, U.S.A.  
nje@astro.as.utexas.edu

JEONG-EUN LEE

Department of Astronomy, The University of Texas at Austin, 1 University Station C1400, Austin, Texas  
78712-0259, U.S.A.  
jelee@astro.as.utexas.edu

JONATHAN M. C. RAWLINGS

Department of Physics and Astronomy, University College London, Gower Street, London WC1E 6BT, UK  
jcr@star.ucl.ac.uk

MINHO CHOI

Taedeuk Radio Astronomy Observatory, Korea Astronomy Observatory, Hwaam 61-1, Yuseong, Daejeon  
305-348, Korea  
minho@trao.re.kr

*Draft version March 27, 2019*

### ABSTRACT

We present observations of 25 transitions of 17 isotopologues of 9 molecules toward B335. With a goal of constraining chemical models of collapsing clouds, we compare our observations, along with data from the literature, to models of chemical abundances. The observed lines are simulated with a Monte Carlo code, which uses various physical models of density and velocity as a function of radius. The dust temperature as a function of radius is calculated self-consistently by a radiative transfer code. The gas temperature is then calculated at each radius, including gas-dust collisions, cosmic rays, photoelectric heating, and molecular cooling. The results provide the input to the Monte Carlo code. We consider both *ad hoc* step function models for chemical abundances and abundances taken from a self-consistent modeling of the evolution of a star-forming core. The step function models can match the observed lines reasonably well, but they require very unlikely combinations of radial variations in chemical abundances. Among the self-consistent chemical models, the observed lines are matched best by models with somewhat enhanced cosmic-ray ionization rates and sulfur abundances. We discuss briefly the steps needed to close the loop on the modeling of dust and gas, including off-center spectra of molecular lines.

*Subject headings:* ISM: abundances — ISM: molecules — ISM: individual (B335) — astrochemistry

### 1. INTRODUCTION

The Bok globule, B335, is a rather round dark globule at a distance of about 250 pc (Tomita et al. 1979). It is perhaps the best case for being a collapsing protostar. Observations of CS and H<sub>2</sub>CO lines (Zhou et al. 1993; Choi et al. 1995) were reproduced very well with models of inside-out collapse (Shu 1977). To the extent that such models may describe the actual density and velocity fields in B335, this source provides an excellent test bed for astrochemical models. The only remaining variables in modeling the lines would be the chemical abundances of the species in question. It is even possible to trace variations in the abundance as a function of radius because the different parts of the line profile arise in different locations along the line of sight. Adding the information from the excitation requirements of different lines provides a probe of the abundance through the static envelope and into the collapsing core of the protostar.

On the other hand, the depletion of molecules that is quite apparent in pre-protostellar cores (e.g., Caselli et al. 2002, Lee et al. 2003) warns us that molecular lines alone may be misleading. In the case of B335, Shirley et al. (2002) found that the Shu infall model that fit the molec-

ular lines (Choi et al. 1995) did not reproduce the dust emission. They found instead that a power law density model with higher densities at all radii than the best fit Shu model was needed to fit the dust emission. We will consider models more similar to the best fitting power law as well.

In general, the molecular lines and dust emission have complementary advantages and disadvantages. The lines can be strongly affected by depletion that varies with radius, while the dust shows no convincing evidence so far for variation of opacities with radius (Shirley et al. 2002). On the other hand, variation in opacities with radius is also not ruled out, and the actual value of the opacity at long wavelengths is quite uncertain, by factors of at least 3 and possibly more. The dust emission is sensitive only to the column density along a line of sight, while the line emission can in principle probe the volume density via excitation analysis. Finally, only the lines can probe the kinematics, but that probe can be confused by depletion effects (Rawlings & Yates 2001), and the dust is needed to constrain these effects. Clearly, the best approach is a unified model for both gas and dust components.

We will present new observations of a large number of species toward B335, using Haystack Observatory and the

Caltech Submillimeter Observatory. We will also present the results of detailed models of radiative transport in dust to determine the dust temperature for several different physical models. Next, we will calculate the gas kinetic temperature, including gas-dust interactions, cosmic rays, and photoelectric heating. With these as a basis, we will calculate the molecular excitation and radiative transport, using a Monte Carlo code (Choi et al. 1995). A telescope simulation code will produce model line profiles, given an input model of the density, temperature, velocity, and abundances as a function of radius, for comparison with the observed line profiles. Based on the comparison, the abundances of various species will be constrained. We will use step function models for the abundances and also the results of new calculations of abundances in a cloud collapsing according to the Shu picture (Lee et al. 2004).

## 2. OBSERVATIONS

We obtained observations of the  $\text{HCO}^+$  and  $\text{N}_2\text{H}^+$   $J = 1 \rightarrow 0$  lines at the Haystack Observatory in 1995 March. Observations of a large number of lines were obtained at the Caltech Submillimeter Observatory in the period 1995 March to 2001 July. Table 1 provides the reference frequency for the line, the telescope, the main beam efficiency ( $\eta_{\text{mb}}$ ), the full width at half maximum beam size ( $\theta_b$ ), the velocity resolution ( $\delta v$ ), and the date of observation. We also provide this information for several observations obtained previously that are used to constrain the modeling. The frequencies in Table 1 are either those used during observing or those used later to shift the observed data to an improved rest frequency. For most lines with hyperfine components, these are the reference frequencies suitable for a list of hyperfine components that were used to fit lines. In the case of the  $\text{N}_2\text{H}^+$   $J = 1 \rightarrow 0$  line, it is the frequency of the isolated hyperfine component, best suited for determining the velocity.

In the following sections, we assume that the centroid of B335 is at  $\alpha = 19^{\text{h}}34^{\text{m}}35.4^{\text{s}}$ ;  $\delta = 07^{\circ}27'24''$  in 1950 coordinates. This position agrees within  $1''$  with the centroid of the submillimeter emission mapped with SCUBA (Shirley et al. 2000). This position was originally based on the position of the millimeter continuum source seen by Chandler & Sargent (1993); more recent interferometric data find a compact component located  $3''.6$  west and  $1''$  south of this position (Wilner et al. 2000). At this position, a continuum source is also seen at 3.6 cm, attributed to a time variable radio jet elongated along the outflow axis (Reipurth et al. 2002). The difference between our position and the position of the compact component is not significant for the resolution of these observations. Some of our data were obtained before we settled on this position. In cases where we have a map, we may have resampled the data spatially to synthesize a spectrum at the submillimeter centroid position, resulting in a slight degradation of the spatial resolution.

## 3. RESULTS

The primary observational results are presented in Table 2 and Figure 1 to Figure 7. The table gives the integrated intensity ( $\int T_A^* dv$ ), the peak antenna temperature ( $T_A^*$ ), the velocity with respect to the local standard of rest ( $v_{\text{LSR}}$ ), and the linewidth (FWHM),  $\Delta v$ . For simple,

single-peaked lines, these were determined from a Gaussian fit. For self-reversed lines without hyperfine structure ( $\text{HCO}^+$   $J = 1 \rightarrow 0$ ,  $J = 3 \rightarrow 2$ , and  $J = 4 \rightarrow 3$ ),  $\int T_A^* dv$  is the total area under the full line,  $T_A^*$  is the strength of the stronger peak,  $v_{\text{LSR}}$  is the velocity of the dip, determined by eye, and  $\Delta v$  is  $\int T_A^* dv$  divided by  $T_A^*$ . For lines with hyperfine structure ( $\text{C}^{17}\text{O}$   $J = 2 \rightarrow 1$ ,  $\text{N}_2\text{D}^+$   $J = 3 \rightarrow 2$ ),  $\int T_A^* dv$  gives the area under all the hyperfine components,  $T_A^*$  gives the peak of the strongest, usually blended components, and  $v_{\text{LSR}}$  and  $\Delta v$  come from a fit with all the hyperfine components. For the most complex situation, lines that are self-reversed, with hyperfine structure, various strategies were adopted. For  $\text{CN}$   $J = 2 \rightarrow 1$ ,  $\int T_A^* dv$ ,  $T_A^*$ , and  $v_{\text{LSR}}$  were determined as for double peaked lines, but  $\Delta v$  was determined from an isolated component. The spectrum of  $\text{CN}$  (Figure 6) clearly shows that the main hyperfine line is self-reversed. For  $\text{N}_2\text{H}^+$   $J = 1 \rightarrow 0$ , all line parameters were determined from the isolated component at the frequency given in Table 1, as suggested by Lee, Myers, & Tafalla (2001).

The observations that are compared to full models are shown as solid lines in Figures 1 to 6. The  $\text{CN}$   $J = 2 \rightarrow 1$  spectrum in Figure 6 has not been modeled, and the dashed line is just a fit to the hyperfine components. Other spectra that are not modeled in detail are shown in Figure 7. These include spectra with complex hyperfine splitting that we cannot model in detail and molecules without good collision rates.

The  $\text{HCN}$   $J = 3 \rightarrow 2$  line is peculiar in that there is essentially no emission at velocities that would normally be associated with the red part of the main hyperfine component. To ensure that this effect was not caused by emission in the off position ( $10'$  west), we took a deep integration in the off position. No emission was seen at a level of 0.08 K.

Single-peaked lines without overlapping hyperfine components provide the best measure of the rest velocity of the cloud. Based on those lines least likely to be optically thick, the cloud velocity is  $\langle v_{\text{LSR}} \rangle = 8.30 \pm 0.05 \text{ km s}^{-1}$ . For self-reversed lines, the mean velocity of the dip (determined by eye) is  $\langle v_{\text{dip}} \rangle = 8.41 \pm 0.06 \text{ km s}^{-1}$ . All the values for  $v_{\text{dip}}$  exceed those for  $\langle v_{\text{LSR}} \rangle$ , by amounts ranging from  $0.05 \text{ km s}^{-1}$  to  $0.25 \text{ km s}^{-1}$ . The mean shift,  $\langle v_{\text{dip}} - \langle v_{\text{LSR}} \rangle \rangle = 0.11 \pm 0.07$ . Also, lines from higher  $J$  levels have higher  $v_{\text{dip}}$  than those from lower  $J$  levels, suggesting that the dip arises partially from inflowing gas. The three lines of  $\text{HCO}^+$ , for example, have their dip at increasing velocity, with the  $J = 4 \rightarrow 3$  showing  $v_{\text{dip}} = 8.55 \text{ km s}^{-1}$ . This progression is similar to a pattern seen in CS lines toward IRAM04191 by Belloche et al. (2002).

## 4. THE MODELING PROCEDURE

We use the extensive observations described above to test models of the source. All the models are spherical models with smooth (non-clumpy) density distributions. We focus on inside-out collapse models, though we discuss some variations on this basic model. All models include self-consistent calculations of the dust and gas temperature distributions (§4.1) and calculations of the molecular populations, radiative transport, and line formation (§4.3). Two kinds of models of the abundances as a function of radius are used: step function models, and abundances from

an evolutionary chemical calculation (Lee et al. 2004), as described in §4.2.

#### 4.1. Determining Temperatures

The first step in comparing a physical model to observations is to determine the temperatures that correspond to a particular density distribution. The dust temperatures can be calculated self-consistently for a particular density distribution by various radiative transfer codes. We used the code of Egan et al. (1988) and the techniques described by Shirley et al. (2002) for constraining parameters.

We assumed that dust opacities are given by column 5 of the table in Ossenkopf & Henning (1994), known as OH5 opacities, because these have been shown to match many observations of star forming cores (e.g., Shirley et al. 2002). One difference between the models by Shirley et al. and the current work is in the treatment of the interstellar radiation field (ISRF). In the previous work, we decreased the strength of the ISRF by a constant factor ( $s_{ISRF}$ ) at all wavelengths (except for the contribution of the cosmic microwave background). For B335, we used  $s_{ISRF} = 0.3$ . In the present work, we instead attenuate the ISRF using the Draine & Lee (1984) extinction law and assuming  $A_V = 1.3$  mag. This procedure affects short wavelengths much more than long wavelengths, leading to a somewhat less pronounced rise in dust temperature toward the outside of the cloud. The choice of  $A_V = 1.3$  mag is somewhat arbitrary, but it accounts for the fact that molecules require some dust shielding. It will also produce consistent results when we consider the gas energetics.

Shirley et al. assumed an outer radius of 60,000 AU for most B335 models. We will mostly use an outer radius of 0.15 pc (31,000 AU), as used by Choi et al. (1995). Studies of the extinction as a function of impact parameter from HST/NICMOS data are consistent with an outer radius of about this size (Harvey et al. 2001), in the sense that the extinction decrease with radius blends into the noise at that radius. The choice of outer radius makes little difference in most models. The inner radius for the dust models is taken to be  $10^{-3}$  of the outer radius for the dust models in order to capture the conversion of short-wavelength radiation from the forming star and disk to longer wavelength radiation. The stellar temperature is set to 6000 K, but this choice is completely irrelevant because of the rapid conversion to longer wavelength radiation. The luminosity was set to  $4.5 L_{\odot}$ , which provided the best fit to a Shu model in Shirley et al. (2002).

Once we have a dust temperature distribution,  $T_d(r)$ , and a density distribution,  $n(r)$ , we can compute the gas temperature distribution,  $T_K(r)$ . This was done with a gas-dust energetics code written by S. Doty [see Doty & Neufeld (1997) and the appendix in Young et al. (2004) for descriptions]. This code includes energy transfer between gas and dust, heating by cosmic rays and the photoelectric effect with PAHs, and molecular cooling.

The gas-dust energy transfer via collisions depends on the total grain cross section per baryon, averaged over the distribution of grain sizes ( $\Sigma_d$ ). Following the discussion in the Appendix of Young et al. (2004), we take this value to be  $6.09 \times 10^{-22}$  cm<sup>2</sup>. The cosmic ray heating depends on the cosmic ray ionization rate ( $\zeta$ ), which we take to be  $3 \times 10^{-17}$  s<sup>-1</sup> (van der Tak & van Dishoeck 2000). The

photoelectric heating follows the equation of Bakes & Tielens (1994), which includes heating from the photoelectric effect on very small grains. The rate depends on the strength of the ultraviolet portion of the ISRF and the electron density. Because this heating is only important on the outside of the cloud, we set the electron density to  $1 \times 10^{-3}$  cm<sup>-3</sup>. The radiation field is assumed to be attenuated by the surrounding medium according to  $\tau_{UV} = 1.8A_V$ ; with  $A_V = 1.3$ , the scale factor for the ISRF impinging on our model's outer radius is  $G_0 = 0.1$ . Once inside the cloud, the radiation is attenuated according to a fit to the attenuation produced by the dust assumed to be in the cloud.

The result of these calculations is shown for a typical model in Fig. 8. For small radii,  $T_K \approx T_d$ , as is usually assumed, but  $T_K$  falls below  $T_d$  with increasing radius, as the density becomes too low for collisions with dust to maintain the kinetic temperature at the dust temperature. Then, at some radius,  $T_K$  rises as photoelectric heating takes over, and  $T_K > T_d$ . The downturn in  $T_K$  at the cloud edge appears to be real and caused by the cooling lines of CO becoming optically thin (see Young et al. 2004). However, this drop in temperature has no appreciable effect on the resulting line profiles.

The amount of photoelectric heating is the least certain of these inputs, as the external attenuation has a large effect on how warm the outer cloud gets. To constrain  $G_0$ , we modeled the lower three lines of CO and compared to data in the literature (e.g., Goldsmith et al. 1984, Langer, Frerking, & Wilson 1986). To avoid producing a CO  $J = 1 \rightarrow 0$  line that exceeded the observations,  $G_0$  definitely needed to be decreased from unity. The value of  $G_0 = 0.1$  provided the best match, and this was actually used to constrain the external extinction to  $A_V = 1.3$ . Changes by a factor of 2 in  $G_0$  (or  $\pm 0.4$  in  $A_V$ ) produced CO lines that differed from the observations by about 30%, while having no appreciable effect on the lines of other species. While other variables are uncertain in the photoelectric heating, the attenuation of the ultraviolet radiation from the ISRF is the most important variable; comparison to observations of CO readily constrain it. The results are reasonable; one does not expect significant molecular gas for  $A_V < 1$  (van Dishoeck & Black 1988). One could trade off the value of  $s_{ISRF}$  and the external extinction, as long as the effective  $G_0$  is not too different from 0.1. Constraining these separately is difficult (Shirley et al. 2004) and not particularly relevant for this paper.

The cooling rates (Doty & Neufeld 1997) depend primarily on the CO abundance and the width of the lines (through trapping); we assume  $X(CO) = 7.4 \times 10^{-5}$  and  $b = 0.12$  km s<sup>-1</sup>, except for some tests described below. We note in passing the dangers of simplistic interpretation of observed CO lines; turning the observations into a kinetic temperature would lead one to conclude that  $T_K$  is constant within the cloud, while it clearly is not.

The parameters that describe the standard physical model are summarized in Table 3.

#### 4.2. Chemical Modeling

Two kinds of abundance models are employed. The first is strictly *ad hoc*, using a step function to describe the abundance of each species as a function of radius. These

models have three free parameters per species:  $X$ ,  $r_{dep}$ , and  $f_{dep}$ . The abundance in the outer parts of the cloud ( $X$ ) is assumed to decrease inside a depletion radius ( $r_{dep}$ ) by a factor ( $f_{dep}$ ).

The second are true chemical models, based on the calculations presented by Lee et al. (2004). These calculations follow the chemical evolution through an evolutionary sequence that includes at each step a self-consistent calculation of the dust and gas temperatures, using the techniques described in the previous section. The evolutionary model assumes a slow build-up in central density, via a sequence of Bonnor-Ebert spheres, to the point of a singular isothermal sphere, at which point, an inside-out collapse (Shu 1977) is initiated. After this point, the chemistry is calculated for each of 512 gas parcels as it falls into the central region. Thus, gas inside the infall radius carries some memory of the conditions from farther out. We adopt the model of Young and Evans (2004) for the evolution of luminosity in order to calculate the evolution of dust temperature. Physical parameters in the model are selected to have a total internal luminosity and a dust temperature profile similar to those obtained from the dust modeling of B335, at the time step of  $r_{inf} = 0.03$  pc. The model core is assumed to stay in the same environment through its evolution with the same  $A_V$  and  $G_0$  calculated in the previous section. The chemical calculation includes the interaction between gas and dust grains as well as gas-phase reactions, but the surface chemistry is not considered in the calculation. For details of the chemical evolution model, refer to Lee et al. (2004).

For both types of models, isotope ratios were constrained so that the abundance was only a free parameter for the whole of the isotope complex.  $\text{DCO}^+$  was the exception, as it is subject to large fractionation effects. Assumed isotope ratios are the same as those used by Jørgensen et al. (2004) and are given in Table 4. Wouterloot et al. (2004) have recently suggested a slightly higher ratio for  $^{18}\text{O}/^{17}\text{O}$  of 4.1, but this value would fit our data on the CO isotopologues somewhat worse.

### 4.3. Modeling of Line Profiles

The line profiles were modeled with a Monte Carlo code (mc) to calculate the excitation of the energy levels and a virtual telescope program (vt) to integrate along the line of sight, convolve with a beam, and match the velocity resolution, spatial resolution, and main beam efficiency of the observations (Choi et al. 1995). All lines were assumed to be centered at  $8.30 \text{ km s}^{-1}$ , based on the average of optically thin lines.

The input physical conditions (density, temperature, and velocity fields) were taken from the physical model being tested, using the results of the gas-dust energetics code for  $T_K(r)$ . Models require input data about each molecule, as well as about the source. For CS, we used collision rates from Turner et al. (1992). For  $\text{HCO}^+$  and  $\text{N}_2\text{H}^+$ , we used collision rates supplied by B. Turner, based on his extension of previously calculated rates to higher temperatures and energy levels (Turner 1995). For  $\text{H}_2\text{CO}$  and para- $\text{H}_2\text{CO}$ , we used rates computed by Green (1991). Rates for HCN came from Green & Thaddeus (1974) and those for CO from Flower & Launay (1985). In some cases, rates have been extrapolated to lower temperatures.

For  $\text{C}^{17}\text{O}$ , HCN, and  $\text{N}_2\text{H}^+$ , the lines have hyperfine structure that is partially resolved. For these lines, mc and vt models were run separately for each clearly resolved hyperfine component, with abundances adjusted to simulate the fraction of the transition probability in that component; the results were added to make the final simulated line. Components separated by less than the  $1/e$  width of the velocity dispersion were aggregated into a single component; the aggregated components are listed in Table 5. This procedure captures the essence of the hyperfine splitting, but it is not rigorous because trapping is not handled correctly when there is partial line overlap (see Keto et al. 2004).

All models were run with 40 shells. The inner radius was  $2 \times 10^{-3}$  pc, corresponding to  $1''.7$  at a distance of 250 pc. This radius is larger than the inner radius for the dust models because the molecular lines are not sensitive to emission from very small scales because of beam dilution. The convergence criterion for populations was set to 10% for finding the region of best-fitting parameters. Final models were run with a 2% convergence criterion to ensure accuracy; differences between these models and those run with 10% accuracy were small. The minimum fractional population tested for convergence was  $10^{-6}$ . For an explanation of these criteria, see the Appendix in Choi et al. (1995).

## 5. INSIDE-OUT COLLAPSE MODELS

The physical properties of the standard model are given in Table 3. The standard physical model is the inside-out collapse model (Shu 1977) that best matched (Choi et al. 1995) the CS and  $\text{H}_2\text{CO}$  data taken by Zhou et al. (1993). Choi et al. (1995) modeled CS and  $\text{H}_2\text{CO}$  lines from the IRAM telescope, assuming constant abundances, and found a best fit  $r_{inf} = 0.03$  pc. This was a compromise, as  $\text{H}_2\text{CO}$  favored smaller  $r_{inf}$  than did CS.

While the CS data were still well matched with constant abundance, the new data on more  $\text{H}_2\text{CO}$  lines suggested enhanced abundances on small scales, as did the  $\text{HCO}^+$  data. As a result, we tested step function abundance models.

### 5.1. Step Function Abundances

To avoid too many free parameters, we required that  $r_{dep} = r_{inf}$ . While this particular choice has no theoretical justification, it leaves only two free parameters per species. With the constraints on isotope ratios in Table 4, we are left with 15 free parameters for 8 species, including the special case of  $\text{DCO}^+$ , explained below. The abundances in Table 6 are those that fit the current data reasonably well, as judged by eye and statistical measures. We calculated both the reduced chi-squared ( $\chi_r^2$ ) and the absolute deviation ( $AD = \sum_i |T_A^*(model; i) - T_A^*(obs; i)|/N$ ) over the line profiles. The absolute deviation is more influenced by strong lines for which the shape is important to match, so we use it primarily, though the  $\chi_r^2$  criterion does not differ in the choice of best model. We have not run a complete grid of models; instead, we employed some judgment to locate regions of parameter space with decent fits to the line profiles. Once reasonably good fits were obtained, both  $X$  and  $f_{dep}$  were varied by factors of 3 in each direction, showing substantially worse fits. These parameters should

be considered constrained at that level. The abundances in Table 6 are those for the best-fitting step functions, and the predicted line profiles are shown in Figures 1 to 6 as gray lines. The values of  $AD$  in Table 6 are an average over all the lines for all isotopologues of that species.

The CS lines were still matched best with constant abundance. On the small scales (0.003 pc) probed by interferometers, the CS is clearly depleted in the envelope and the  $J = 5 \rightarrow 4$  emission arises from a clump that is offset from the central source (Wilner et al. 2000). A model with CS depleted by a factor of 10 for  $r_{dep} = 0.003$  pc showed no appreciable effect on the  $J = 2 \rightarrow 1$  or  $J = 3 \rightarrow 2$  lines, but it did decrease the predicted  $J = 5 \rightarrow 4$  intensity slightly.

The H<sub>2</sub>CO abundance that best fits the data is slightly higher than was found by Choi et al. (1995), mostly to improve the fit to the lines of H<sub>2</sub><sup>13</sup>CO and para-H<sub>2</sub><sup>13</sup>CO. We also increased the abundance of both H<sub>2</sub>CO and para-H<sub>2</sub>CO in the inner parts of the cloud to improve the fit to our new CSO observations of the higher-J lines, whereas Choi et al. (1995) had found a constant abundance to be satisfactory. Even so, we do not reproduce the very high excitation H<sub>2</sub>CO lines, indicating that a warm, dense region must exist that is not predicted by the basic model.

The abundance of H<sub>2</sub>CO listed in Table 6 is actually the abundance of ortho-H<sub>2</sub>CO. Minh et al. (1995) found that ortho-H<sub>2</sub>CO/para-H<sub>2</sub>CO was 1.7 in B335, assuming a uniform cloud. Our modeling, which employs density, temperature, and velocity gradients, confirms that this ratio works well in reproducing the observations, but we have not determined the range of acceptable values. Minh et al. (1995) noted that this ratio was consistent with ortho-para equilibration on cold dust grains and suggested that the gas-phase H<sub>2</sub>CO in B335 had formerly resided on dust grains. In this picture, they suggested that warming by the newly-formed star or by shocks had liberated the H<sub>2</sub>CO from the dust grains. Our model for the dust temperature indicates that  $T_d$  stays below 20 K until  $r < 0.006$  pc (6''), where any H<sub>2</sub>CO would be beam diluted. Thus, other means for releasing the H<sub>2</sub>CO from dust mantles should be explored.

The lines of HCO<sup>+</sup> and its isotopologues are best matched with a model with increased abundances inside  $r_{inf}$ . HCO<sup>+</sup> is clearly quite abundant in B335, as witnessed by the detection of HC<sup>18</sup>O<sup>+</sup>. The observed  $J = 3 \rightarrow 2$  and  $J = 4 \rightarrow 3$  lines of HCO<sup>+</sup> are somewhat weaker than the models predict and the dip is shifted to the red (§5.2). The abundance of DCO<sup>+</sup> was treated as a free parameter but  $r_{dep}$  and  $f_{dep}$  were constrained to the same value as for HCO<sup>+</sup>; the best fit was obtained for HCO<sup>+</sup>/DCO<sup>+</sup> of 55.

The C<sup>18</sup>O lines were fitted best with decreased abundances (but only by a factor of 3) inside  $r_{inf}$ . With the enforced C<sup>18</sup>O/C<sup>17</sup>O ratio of 3.5, the C<sup>17</sup>O model line is a bit weaker than the observed line, but the data are rather noisy. Using the standard isotope ratio, the best fit abundance of C<sup>18</sup>O would imply  $X(CO) = 4 \times 10^{-5}$ . This abundance is substantially less than expected from chemical models and even less than what we assume in our calculation of cooling rates (§4.1). To see the consequences, we ran a model with the abundance adjusted to this value in the calculation of cooling rates. The value of

$T_K$  in the outer parts of the cloud was increased by a few degrees, but the effect on most molecular lines was very small, indicating that the best fit is not affected by this slight inconsistency. The CO line predictions were exceptions, as these lines actually got *stronger* with *decreased* CO abundance because of the higher  $T_K$  in the relevant layers of the cloud.

The two lines of N<sub>2</sub>H<sup>+</sup> both have hyperfine structure and our method for dealing with this is only approximate. Nonetheless, the  $J = 1 \rightarrow 0$  transition is matched reasonably well (Fig. 6) with a factor of 10 increase in abundance inside  $r_{inf}$ . In contrast, the satellite hyperfine lines of the  $J = 3 \rightarrow 2$  line are clearly stronger than the models can explain.

The most troublesome species was HCN. The satellite hyperfine lines of both  $J = 1 \rightarrow 0$  and  $J = 3 \rightarrow 2$  transitions are much stronger than the models can account for, even with a very large HCN abundance. Still larger abundances predicted lines of the stronger hyperfine components that were much stronger than observed. In addition, the HCN  $J = 3 \rightarrow 2$  line is very peculiar, with the red side of the line essentially missing, indicative of a deep absorption layer. To try to match some of these features within the constraints of our model, we depleted HCN by a factor of 10 inside  $r_{inf}$ . This helped, but the fits are still poor. The fact that the H<sup>13</sup>CN  $J = 3 \rightarrow 2$  line was not detected makes the strength of the hyperfine satellite lines (Fig. 7) even harder to understand.

## 5.2. Variations in the Physical Model

With the additional freedom of the step function abundance profile, is  $r_{inf} = 0.03$  pc still the best model? This question was explored to a limited degree; for each new  $r_{inf}$ , the abundances of each species were optimized, but the shape of the step function was not allowed to change, except for CS, where changes in  $f_{dep}$  were allowed. For modest changes ( $r_{inf} = 0.02 - 0.04$  pc), the overall fits were not much worse. As found by Choi et al. (1995), the CS favored  $r_{inf} = 0.03$  pc, while H<sub>2</sub>CO favored smaller  $r_{inf}$ . For factor of 3 changes, the fit degraded substantially (Fig. 9). For  $r_{inf} = 0.01$  pc, optically thick lines were too narrow and the two peaks were nearly equal in strength, unlike the observations. For  $r_{inf} = 0.09$  pc, those lines were too wide and the blue/red ratio was too large. There was also a greater conflict between the requirements of optically thick and optically thin lines; if the abundance was increased to match the latter, the former became too strong. Within the constraints on abundances that we imposed, infall radii different by a factor of 3 would be strongly ruled out. The mean absolute deviations over *all* species ( $\langle AD \rangle$ ) for these different models are listed in Table 7.

The constraints on the infall radius from the molecular line observations are inconsistent with those found by modeling the continuum emission (Shirley et al. 2002). The predicted intensity profiles of the model from Choi et al. (1995) were too flat to match the observations at 850 and 450  $\mu\text{m}$  (see Fig. 6 and Table 3 of Shirley et al 2002). To make an inside-out collapse model fit the data, Shirley et al. had to use a very small infall radius,  $r = 0.0048$  pc, more than 6 times smaller than the infall radius that matches the line profiles. Our modeling confirms that this

small infall radius cannot match the line profiles. This fundamental discrepancy between the models of the dust and molecular line emission will be discussed further in §6.

Harvey et al. (2001) found that an inside-out collapse model with  $r_{inf} \sim 0.03$  pc fit the extinction data well, but only if the density was increased everywhere by a factor of about 5. We tried this model; decreases in abundances by about an order of magnitude were required for most species to bring line strengths back to near observed values. We had to decrease the CS abundance within  $r_{dep}$  to match the data, but this change is not unreasonable. The average deviation is somewhat larger than the standard model, but not terrible. Without constraints on abundances, it is hard to rule out variations in the physical model of this magnitude. However, the shapes of the CS lines were not reproduced well (top panel in Fig. 9), with blue/red ratios clearly less than the observations.

Moving farther afield, one may consider other collapse models. In some sense, the opposite extreme to the Shu (1977) model is the Larson-Penston similarity solution (Larson 1969, Penston 1969). Line profiles from this model were generated by Zhou (1992) and found to be considerably wider than those observed in regions of low-mass star formation. More recently, Masunaga et al. (1998) have shown that radiation hydrodynamical (RHD) calculations of collapse are well approximated by a modified Larson-Penston model. This model produces lower infall velocities than the original Larson-Penston model, which decrease with radius. Masunaga & Inutsuka (2000) have simulated line profiles from the RHD models, finding blue profiles and smaller linewidths, qualitatively consistent with those seen in low mass cores. While these models may indeed have application in some regions, the linewidths listed in Table 4 of their paper for models after formation of the central core are larger than those in B335 by factors of at least two.

There are hints in the spectra of deviations from the Shu model, particularly in the shift of  $v_{dip}$  to higher velocity for lines of higher excitation. This shift can be seen more clearly in Figure 10, where three lines of  $\text{HCO}^+$  are shown. The best step function model is also shown; it does not reproduce this shift. The dip is caused by absorption from low-excitation material. In the Shu model, the outer, static envelope is dominating this absorption. A model with inward motion in this outer layer might better reproduce this shift.

### 5.3. Self-consistent Chemical Models

The chemical models are constrained by assuming an entire evolutionary history for the core, as detailed by Lee et al. (2004). We consider only their standard model of the evolution of physical conditions and luminosity to define the physical conditions, including the dust temperature profile, at the time step for which  $r_{inf} = 0.03$  pc. Compared to the standard model of Lee et al., we allowed adjustment of only 3 free parameters: the binding energy to the dust, set by the assumed nature of the dust surface; the initial abundance of elemental sulfur; and the cosmic-ray ionization rate. The different models are summarized in Table 8.

First, binding energies of molecules onto three different dust grain surfaces were checked. For this comparison, the

initial elemental abundances and the cosmic-ray ionization rate were the same as those in the standard model of Lee et al. (2004). For the CS lines, the binding energy onto a CO-dominant grain mantle works the best and the value of  $\langle AD \rangle$  is slightly better than for  $\text{SiO}_2$ . However, the low binding energy of molecules onto the CO mantle leads to less freeze-out of CO, and, in turn,  $\text{N}_2\text{H}^+$  is destroyed by abundant CO in the gas phase. As a result, simulated CO isotopologue lines are too strong, and simulated  $\text{N}_2\text{H}^+$  lines are too weak compared to the observations. Attempts to improve the fit by reducing the initial abundance of carbon make the fit to CS worse while still not making the models fit CO and  $\text{N}_2\text{H}^+$  profiles.

At the other extreme, CO and CS are frozen-out significantly onto  $\text{H}_2\text{O}$ -dominant grain mantles to produce much weaker lines than the observations indicate.  $\text{HCO}^+$ , which is a daughter molecule of CO, is also depleted from the gas phase. Although  $\text{N}_2\text{H}^+$  is less likely to be destroyed by CO, even nitrogen molecules are easily frozen-out on the  $\text{H}_2\text{O}$  mantle, decreasing the  $\text{N}_2\text{H}^+$  abundance. In addition, HCN increases by 3 orders of magnitude at radii smaller than 0.004 pc, compared to the abundance in the outer regions, giving a very broad line wing, which is not present in the observed lines. Except for weaker CS lines, the lines simulated with abundance profiles calculated for bare  $\text{SiO}_2$  grain surfaces show much better fits to actual data than do those from other assumptions about grain surfaces.

We adopt the bare  $\text{SiO}_2$  grain surface as our standard. In this model, the CO evaporation radius is about 0.006 pc. At radii less than this radius, almost all CO is desorbed from dust grain surfaces. Next, we varied the initial abundance of sulfur to improve the fit to the CS lines. An increase of the initial sulfur abundance by a factor of 5 gives the best results with the  $\text{SiO}_2$  grain surfaces. Other molecular lines do not vary much with the initial abundance of sulfur. The abundance profiles of this model are shown as solid lines in Figure 11. In all chemical models, the  $\text{N}_2\text{H}^+$  and  $\text{HCO}^+$  lines are weaker than the observed lines, so we tested various cosmic-ray ionization rates. A cosmic-ray ionization rate increased by a factor of 2 produced the best fit for  $\text{N}_2\text{H}^+$  and  $\text{HCO}^+$  lines. We increased the ionization rate in the energetics calculation for consistency. HCN lines become stronger with the cosmic-ray ionization rate, and  $\langle AD \rangle$  becomes somewhat worse if we increase the ionization rate by a factor of 5. The abundances for the model with ionization enhanced by a factor of 2 are shown by the dotted lines in Figure 11.

The chemical models produce abundances with large (many orders of magnitude) variations with radius and quite complex radial structure. For explanations of these effects, see Lee et al. (2004). Note in particular the large decreases in abundance at large radii for most species caused by photo-dissociation. The large decrease in CO abundance over a wide range of radii reflects freeze-out onto grain surfaces, and some other species follow this trend, but  $\text{N}_2\text{H}^+$  behaves oppositely because CO destroys  $\text{N}_2\text{H}^+$ . Likewise, most species show a peak at small radii, where CO evaporates, because those species also evaporate there, while  $\text{N}_2\text{H}^+$  decreases when CO evaporates. The abundances for the step function model are also shown in Figure 11. In some cases, they are dramatically different.

The line profiles resulting from the best fit chemical model are shown in Figures 1 to 6 as dotted lines. The average values of absolute deviation for the best chemical model are also listed in Table 6 for comparison to those from the step function models. In most cases, the values of  $AD$  are slightly worse, most notably for  $\text{DCO}^+$  and  $\text{H}_2\text{CO}$ , but many are similar to those of the step function models. Compared to the best fit with step function abundances, the best fit with chemical abundances shows less deep absorption dips in the CS lines, weaker lines of the higher transitions in  $\text{N}_2\text{H}^+$  and  $\text{H}_2\text{CO}$ , and less blue asymmetry in  $\text{HCO}^+$  lines. In addition, the predicted lines of  $\text{HCO}^+$  isotopologues are weaker than in the step function models. To match the observations, the isotope ratios would need to be increased by factors of 3 to 5. The deuterium ratio for the  $\text{DCO}^+$  3–2 would also need to be increased by a factor of 5 to match the observed line. These discrepancies result from the fact that B335 has quite strong lines of rare isotopologues of  $\text{HCO}^+$ . However, standard isotope ratios for  $\text{C}^{18}\text{O}$ ,  $^{13}\text{CO}$ , and  $\text{C}^{17}\text{O}$ , or  $\text{H}_2\text{CO}$  and  $\text{H}_2^{13}\text{CO}$  produce reasonably good matches to the observations. Chemical abundances predict still weaker  $\text{H}_2\text{CO}$  lines in high excitation transitions than do step function abundances. As mentioned in §5.1, higher densities at small radii are necessary to account for the weak high excitation  $\text{H}_2\text{CO}$  lines. Also, the  $\text{N}_2\text{H}^+$  3–2 line is relatively weaker than the 1–0 line when compared to the observed lines, again suggesting the presence of higher densities at small radii.  $\text{HCO}^+$  and HCN lines simulated with chemical abundances are narrower than the observed lines. These two molecules are abundant in outflowing gas. Therefore, the lines might be affected by the outflow, which is not considered in this work. The satellite hyperfine lines of HCN 1–0 are produced better with the abundance profile from the chemical model than with a step function. However, even chemical abundances cannot predict the satellite hyperfine lines of the HCN 3–2 as well as the absence of the red component of the main group. This result suggests the existence of a region with very high HCN abundance. The chemical models also do not reproduce the shift of  $v_{dip}$  with increasing  $J$  seen in the  $\text{HCO}^+$  (Fig. 10).

We also tested different time steps in the same luminosity model. In time steps earlier than the time step for  $r_{inf} = 0.03$  pc, the model core has higher densities at small radii, and the total internal luminosity is smaller than observed for B335 and vice versa for  $r_{inf} > 0.03$  pc. According to the test,  $\text{H}_2\text{CO}$  and  $\text{N}_2\text{H}^+$  lines are fitted much better with the chemical abundances in an earlier time step for  $r_{inf} = 0.015$  pc. The satellite hyperfine lines of the HCN 3–2 are also well fitted, while its main group is too strong. Higher densities at small radii cause these results. In addition, at this time, the CO evaporation radius is about 0.004 pc, so less CO evaporates compared to the time step for  $r_{inf} = 0.03$  pc. As a result,  $\text{N}_2\text{H}^+$  is more abundant. However, at this time, the infall velocities are not big enough to produce the degree of the blue asymmetry in CS lines. The CS lines predicted by models with three times smaller and larger  $r_{inf}$  are also shown in Figure 9 and the values of  $\langle AD \rangle$  are given in Table 7; unlike the step function models, the luminosity is different for these other values of  $r_{inf}$ , because the luminosity increases with time. Nonetheless, similar problems to those

encountered in the step function models appear at earlier and later times.

## 6. DISCUSSION

Both step function models and evolutionary chemical models do a reasonable job of fitting most of the data. Models with constant abundances are not adequate for fitting most observations. In addition, the evolutionary chemical models clearly indicate that abundances vary by orders of magnitude as a result of freeze-out and desorption (Lee et al. 2004). These conclusions are similar to those of Jørgensen et al. (2004), who find that constant abundance models are unsatisfactory and that a drop function works better. The drop function, though simpler, is similar in shape to the abundance profile of CO in Figure 11. It allows a region of lower abundance at intermediate radii and a return to high abundances at small radii. The drop function cannot of course capture the full complexity of the abundance profiles in Figure 11.

Both models fit the CS lines despite the very different radial dependences of the CS abundance. The  $\text{H}_2\text{CO}$  lines are better fitted by the step function models, primarily because they allow a high abundance over a substantial range of radii, where the density is high, thus providing stronger lines of high-excitation transitions. Similarly, the chemical models, even with enhanced ionization, cannot produce sufficient  $\text{HCO}^+$  to match the observations of rare isotopologues. Interestingly, the chemical models do better on the HCN  $J = 1 \rightarrow 0$  line, but neither model can match the peculiar  $J = 3 \rightarrow 2$  line profile.

In comparing models, one should bear in mind that the step function models were allowed 15 free parameters, while the chemical models enjoyed only 3, and those were restricted by prior knowledge. In fact, the step function abundances that fit best are very inconsistent with what we know of chemistry. The CO abundance is depleted inside  $r_{inf}$ , while the  $\text{HCO}^+$  and  $\text{H}_2\text{CO}$  abundances increase; this combination is highly unlikely, especially for  $\text{HCO}^+$ , which is a direct product of CO. The very high abundance of  $\text{HCO}^+$  inside  $r_{inf}$  invoked by the step function models to match the strong lines of rare isotopologues is very hard to produce in any chemical model.

The evolutionary model does not include grain surface reactions, so it does not predict an ortho-para ratio for  $\text{H}_2\text{CO}$ ; we assumed a ratio of 1.7. The most likely route for modifications to the chemical models is to add grain surface reactions, but this step will effectively add many free parameters to the chemical model because rates for surface reactions are poorly known.

On the whole, it is in fact rather remarkable that the line profiles from the self-consistent chemical models are as close as they are to the observations. With variations in abundances of many orders of magnitude with radius, they could easily have failed to match observations by orders of magnitude. In addition, B335 is only one source, and it has a rather rich spectrum for a low mass core, including unusually strong lines of  $\text{HC}^{18}\text{O}^+$ . Of course, this feature makes B335 an attractive source to test theories, but it also may mean that it is atypical.

What can explain the remaining differences between the models and the data? First, the Shu (1977) model of the infall may not be correct. There is a hint in this direction

in the fact that the models do not reproduce the shift of  $v_{dip}$  to the red of  $v_{LSR}$  for optically thin lines (Fig. 10). This result suggests that the outer envelope is not stationary, as in the Shu solution, but is also moving inward. Second, the outflow is not considered in these models, but it will affect abundances and line profiles. To include the outflow, we must move beyond 1-D models. Third, the chemical models may not yet include enough processes for desorption of gas from grain mantles. These could increase the abundances at intermediate radii.

### 6.1. Off-Center Spectra

We have focused here on spectra toward the center of B335. The large differences between the empirical and evolutionary models in the abundances of some species at larger radii suggest that spectra off the center of B335 may help in testing chemical models. Figure 12 shows a sample of spectra at positions off the center predicted by the best-fit empirical and evolutionary models. For  $\text{HCO}^+$  and  $\text{C}^{18}\text{O}$ , we show observed spectra at these positions, produced by averaging spectra displaced in all directions with that separation in our maps. We also show predictions of CS spectra displaced by  $60''$ ; we no longer have the observed spectra at those positions, but they are presented by Zhou et al. (1993). For the  $\text{HCO}^+ J = 4 \rightarrow 3$  line, the evolutionary model gives a weaker line, closer to the observations, than the empirical model at  $15''$  offset. Conversely, the evolutionary model produces stronger lines of  $\text{C}^{18}\text{O}$  at  $30''$  offset than either the empirical model or the data. The differences are most dramatic for CS lines  $60''$  away from the center. The strong decrease in CS abundance in the evolutionary models, seen in Fig. 11, produces lines that are much weaker than those of the empirical model. Zhou et al. (1993) detected lines stronger than either prediction, but the noise was fairly high. Improved maps of CS with good spatial resolution would be very helpful in further constraining models. The decrease in CS abundance at large radii is quite sensitive to the external extinction (see Fig. 13 of Lee et al. 2004). Models with higher values of external extinction, but with all other parameters unchanged, do greatly increase the strength of CS lines at off-center positions. Maps of appropriate lines can help to constrain the environment of the core, while observations with much higher resolution can test the predictions of abundance peaks at small radii (Lee, Evans, & Bergin 2005).

### 6.2. What about the Dust?

We noted above that the molecular line emission and the dust emission lead to inconsistent conclusions about the density distribution. To summarize, the dust emission data is consistent with an inside-out collapse model only if the infall radius is much smaller than the molecular line data indicate (Shirley et al. 2002). Attempts to adjust abundances to make the line profiles predicted for the small infall radius match the observations failed; the predicted line profiles are simply too narrow at the early times implied by the small infall radius.

The other possibility is that the model based on the dust emission is wrong. While Shirley et al. performed an extensive set of tests, there are two possibilities that remain to be considered: changes in the dust opacity as a

function of radius; and contributions to the dust emission from a disk. Both of these would work by adding flux at small radii, steepening the predicted radial intensity profile. For example, Young et al. (2003) found that one could overestimate  $p$ , the best-fit exponent in a power-law model by up to 0.5, if the contribution of a disk was ignored. This difference could change the best-fit value of  $p = 1.8$  to something more compatible with the inner part of an inside-out collapse.

In fact, Harvey et al. (2004) have found evidence for a disk in B335 and modeled multi-configuration data from the IRAM Plateau de Bure Interferometer with an envelope-disk combination. They find a good fit with a disk producing a flux of 21 mJy at 1.2 mm and an envelope with a broken power law:  $n = 3.3 \times 10^4 (r/r_b)^{-1.5}$  for  $r < r_b$ ; and  $n = 3.3 \times 10^4 (r/r_b)^{-2.0}$  for  $r > r_b$ . The best fit  $r_b$  is 0.032 pc, essentially the same as our best fit for the infall radius, and the two broken power laws agree with the inside-out model for  $r > r_{inf}$ , and with the asymptotic behavior of inside-out collapse at small radii. However, the density just inside the infall radius has a slower dependence on  $r$  in the inside-out collapse solution; Harvey et al. (2004) note that this theoretical  $n(r)$  does not fit their data well.

We have scaled up the flux of the disk in the Harvey et al. (2004) model ( $S_\nu \propto \nu^3$ ) and modeled the 850 and  $450 \mu\text{m}$  data from Shirley et al. (2000) with an inside-out collapse model and a point source with the flux of the disk. The intensity profiles are not well-fitted unless the point source is 5-10 times stronger than in the Harvey et al. model. Models with disks and radial variations in dust opacity are needed to resolve these questions, but they are outside the scope of this paper.

We conclude that the issues of disks (or more generally, compact structure) and radial variations in dust opacity introduce enough uncertainty that it is not yet possible to close the loop fully on the modeling of molecular lines and dust continuum.

## 7. CONCLUSIONS

We have assembled data on a large number of molecular lines toward B335 and compared those lines to predictions of models. The models are of two primary types: those with step function chemical abundances and those with chemical abundances resulting from an evolutionary calculation (Lee et al. 2004). In both cases, the temperatures of dust and gas are calculated from the luminosity of the protostar and the density distribution under study. In both cases, the underlying physical model is the inside-out collapse model of Shu (1977).

Both step function and evolutionary chemical abundances can fit most of the data, with some residual puzzles remaining. Both favor an infall radius around 0.03 pc, as was found from earlier modeling by Zhou et al. (1993) and Choi et al. (1995). Models with the same infall radius, but with densities enhanced by a factor of 5, as suggested by Harvey et al. (2001) do not fit as well, but they cannot be ruled out. Models with much smaller infall radii, as favored by the dust continuum modeling (Shirley et al. 2002) do not fit the data well at all. Resolving this discrepancy between the conclusions of modeling dust and gas may require modifications to the dust models, includ-

ing incorporation of compact sources and changes in the dust opacities with radius.

The standard chemical evolution model shows huge variations in abundance as a function of radius (Fig. 11 and Lee et al. 2004), but still comes reasonably close to matching the observations. This is quite a remarkable fact. Changes to the initial sulfur abundance and cosmic ray ionization rate improve the fit to the lines, but these may simply be compensating for remaining unknowns in the chemistry. Rawlings and Yates (2001) have highlighted the extreme sensitivity of some abundances and line profiles to free parameters, especially the early evolutionary history. Accordingly, the reader is cautioned that other combinations of history, dynamics, and chemical parameters that we have not explored might also produce reasonable fits to the data. The important point is that chemical models now come close enough that one can begin to look in detail at what might improve the match. However, this should be done after more than one source is compared to the models, as there will be variations in conditions and evolutionary history from source to source.

In addition, the standard physical model of inside-out

collapse does a remarkably good job of predicting the line profiles. However, there are clear hints of dynamics beyond the standard model in the shift of the velocity of the self-absorption dip to higher velocities in lines requiring higher excitation. Models with envelopes moving inward may be more successful in reproducing these features. Spectra at positions away from the center can constrain other parameters, especially the surrounding radiation environment. However, future work should also account for the non-sphericity and other effects of the outflow in this source. Further observations with better spatial resolution will be important to constrain these models, as the line profiles become more diagnostic of both dynamics (Choi 2002) and chemistry (Lee et al. 2004).

We thank the referee for perceptive comments that led to improvements in the paper. We thank Y. Wang, who collected the Haystack data and who was involved in the initial work on this project. We also thank Y-S. Park and W. Irvine for supplying data from their papers. This research was supported in part by NSF grants AST-9988230 and AST-0307250 to the University of Texas at Austin.

#### REFERENCES

- Bakes, E. L. O. & Tielens, A. G. G. M. 1994, *ApJ*, 427, 822  
 Belloche, A., André, P., Despois, D., & Blinder, S. 2002, *A&A*, 393, 927  
 Caselli, P., Walmsley, C. M., Zucconi, A., Tafalla, M., Dore, L., & Myers, P. C. 2002, *ApJ*, 565, 331  
 Chandler, C. J. & Sargent, A. I. 1993, *ApJ*, 414, L29  
 Choi, M. 2002, *ApJ*, 575, 900  
 Choi, M., Evans, N. J., II, Gregersen, E. M., & Wang, Y. 1995, *ApJ*, 448, 742  
 Doty, S. D. & Neufeld, D. A. 1997, *ApJ*, 489, 122  
 Egan, M. P., Leung, C. M., & Spagna, G. R. 1988, *Comput. Phys. Comm.*, 48, 271  
 Flower, D. R. & Launay, J. M. 1985, *MNRAS*, 214, 271  
 Goldsmith, P. F., Snell, R. L., Hemeon-Heyer, M., & Langer, W. D. 1984, *ApJ*, 286, 599  
 Green, S. 1991, *ApJS*, 76, 979  
 Green, S. & Thaddeus, P. 1974, *ApJ*, 191, 653  
 Jørgensen, J. K., Schöier, F. L., & van Dishoeck, E. F. 2004, *A&A*, 416, 603  
 Harvey, D. W. A., Wilner, D. J., Lada, C. J., Myers, P. C., Alves, J. F., & Chen, H. 2001, *ApJ*, 563, 903  
 Harvey, D. W. A., Wilner, D. J., Myers, P. C., & Tafalla, M. 2003, *ApJ*, 596, 383  
 Keto, E., Rybicki, G. B., Bergin, E. A., & Plume, R. 2004, *ApJ*, 613, 355  
 Ladd, E. F., Fuller, G. A., & Deane, J. R. 1998, *ApJ*, 495, 871  
 Larson, R. B. 1969, *MNRAS*, 145, 271  
 Lee, C. W., Myers, P. C., & Tafalla, M. 2001, *ApJS*, 136, 703  
 Lee, J.-E., Evans, N. J., II, Shirley, Y. L., & Tatematsu, K. 2003, *ApJ*, 583, 789  
 Lee, J.-E., Bergin, E. A., & Evans, N. J., II 2004, *ApJ*, 617, 360  
 Lee, J.-E., Evans, N. J., II, & Bergin, E. A. 2005, in prep.  
 Masunaga, H. & Inutsuka, S. 2000, *ApJ*, 536, 406  
 Masunaga, H., Miyama, S. M., & Inutsuka, S. 1998, *ApJ*, 495, 346  
 ApJ, 217, 425  
 Minh, Y. C., Dickens, J. E., Irvine, W. M., & McGonagle, D. 1995, *A&A*, 298, 213  
 Park, Y.-S., Kim, J., & Minh, Y. C. 1999, *ApJ*, 520, 223  
 Penston, M. V. 1969, *MNRAS*, 144, 425  
 Ossenkopf, V. & Henning, Th. 1994, *A&A*, 291, 943  
 Rawlings, J. M. C., Hartquist, T. W., Menten, K. M., & Williams, D. A. 1992, *MNRAS*, 255, 471  
 Rawlings, J. M. C. & Yates, J. A. 2001, *MNRAS*, 326, 1423  
 Reipurth, B., Rodríguez, L., Anglada, G., & Bally, J. 2002, *AJ*, 124, 1045  
 Shirley, Y. L., Evans, N. J., II, Rawlings, J. M. C., & Gregersen, E. M. 2000, *ApJS*, 131, 249  
 Shirley, Y. L., Evans, N. J., II, & Rawlings, J. M. C. 2002, *ApJ*, 575, 337  
 Shirley, Y. L., Nordhaus, M. K., Grcevich, J. M., Evans, N. J., II, Rawlings, J. M. C., & Tatematsu, K. 2004, submitted.  
 Shu, F. H. 1977, *ApJ*, 214, 488  
 Tomita, Y., Saito, T., & Ohtani, H. 1979, *PASJ*, 31, 407  
 Turner, B. E. 1995, *ApJ*, 449, 635  
 Turner, B. E., Chan, K., Green, S., & Lubowich, D. A. 1992, *ApJ*, 399, 114  
 van der Tak, F. F. S. & van Dishoeck, E. F. 2000, *A&A*, 358, L79  
 van Dishoeck, E. F. & Black, J. H. 1988, *ApJ*, 334, 771  
 Wilner, D. J., Myers, P. C., Mardones, D., & Tafalla, M. 2000, *ApJ*, 554, L69  
 Wouterloot, J. G. A., Brand, J., & Henkel, C. 2004, *A&A*, in press  
 Young, C. H., & Evans, N. J., II, *ApJ*, submitted  
 Young, C. H., Shirley, Y. L., Evans, N. J., II, & Rawlings, J. M. C. 2003, *ApJS*, 145, 111  
 Young, K. E., Lee, J.-E., Evans, N. J., II, Goldsmith, P. F., & Doty, S. D. 2004, *ApJ*, 614, 252  
 Zhou, S. 1992, *ApJ*, 394, 204  
 Zhou, S., Evans, N. J., II, Kömpe, C., & Walmsley, C. M. 1993, *ApJ*, 404, 232  
 Zhou, S., Evans, N. J., II, Butner, H. M., Kutner, M. L., Leung, C. M., & Mundy, L. G. 1990, *ApJ*, 363, 168

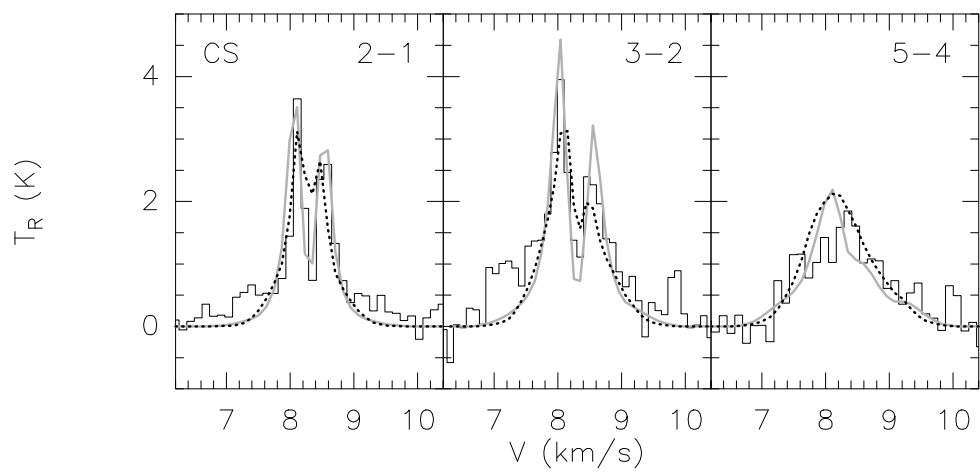


FIG. 1.— Observations of the CS lines observed at IRAM (Zhou et al. 1993) (black solid histogram). The gray solid line is for the model with the step function abundance, and the dotted line shows the model with the chemical abundance.

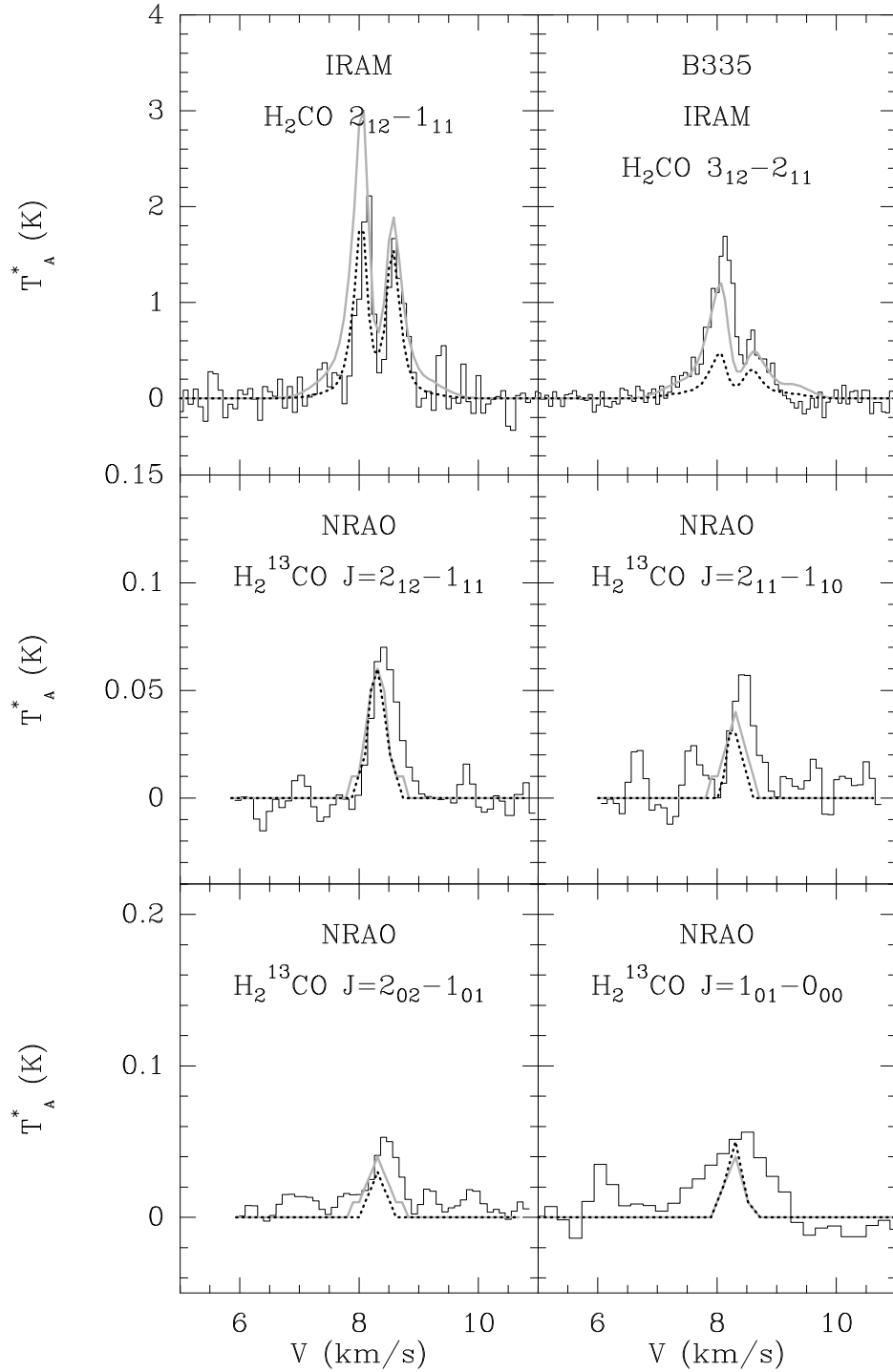


FIG. 2.— The observations of H<sub>2</sub>CO are shown as black solid histograms and the models are shown as gray solid lines (step functions) and dotted lines (chemical abundances). The telescopes where the data were obtained are identified in each panel. The IRAM data were taken from Zhou et al. (1993) and the NRAO data were supplied by W. Irvine, based on data in Minh et al. (1995). The bottom two panels are para-H<sub>2</sub><sup>13</sup>CO.

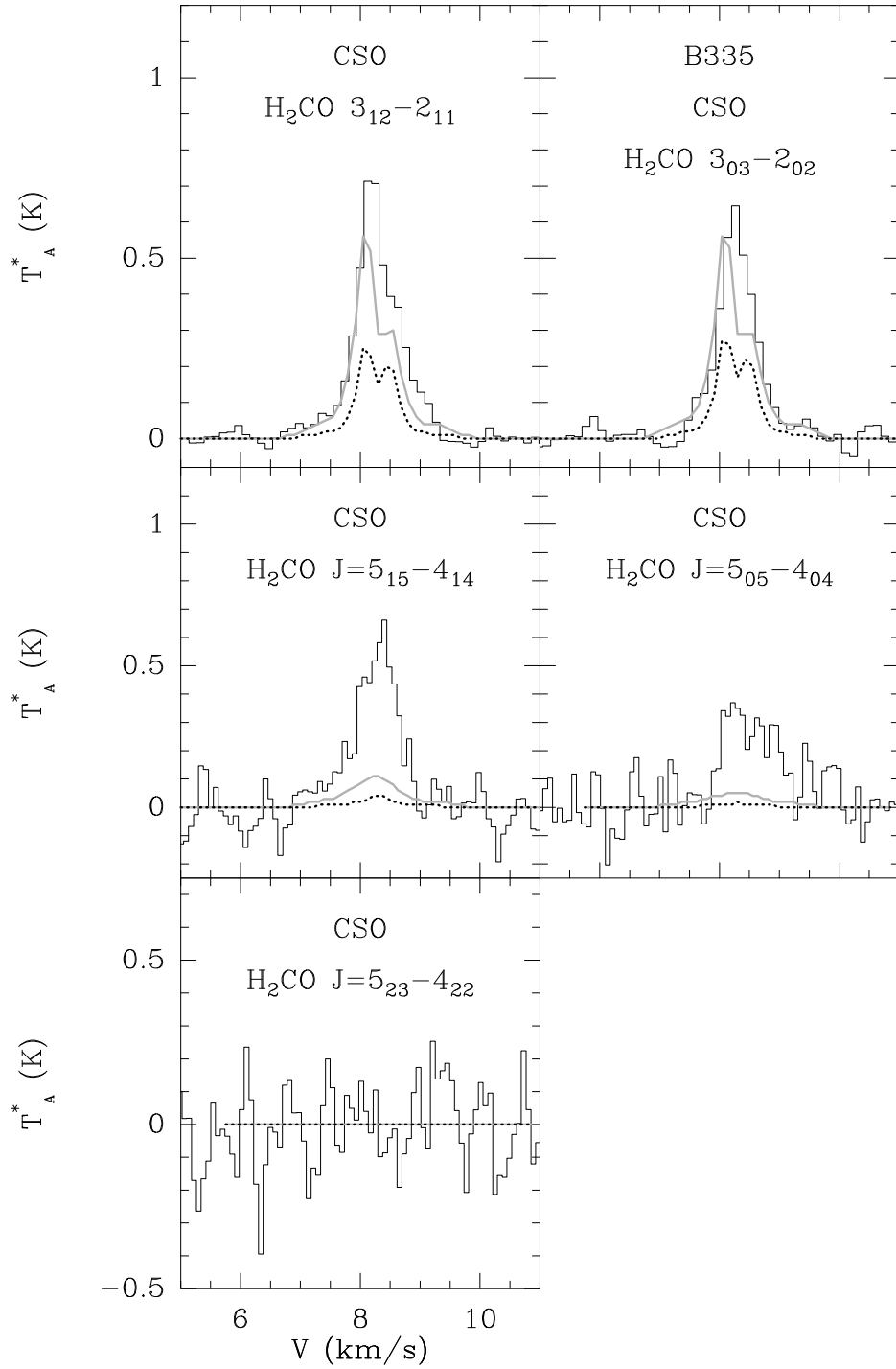


FIG. 3.— Further observations of  $\text{H}_2\text{CO}$  are shown as black solid histograms and the models are shown as gray solid lines and dotted lines. The telescopes where the data were obtained are identified in each panel.

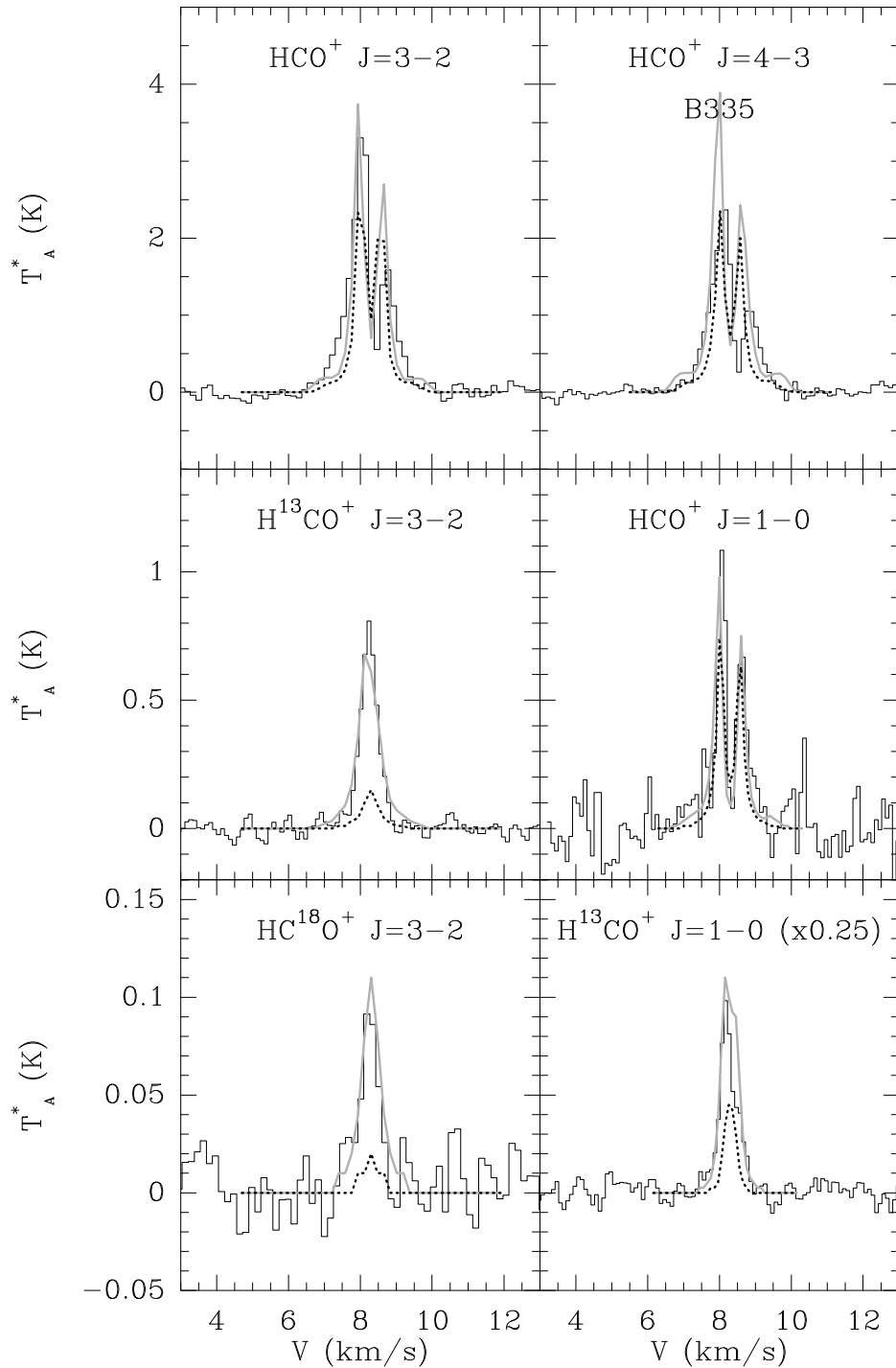


FIG. 4.— The observations of HCO<sup>+</sup> are shown as black solid histograms and the models are shown as gray solid lines (step functions) and dotted lines (chemical abundances). The  $J = 1 \rightarrow 0$  lines were obtained at Haystack and the other lines were obtained at the CSO. Both model and observations of the H<sup>13</sup>CO<sup>+</sup>  $J = 1 \rightarrow 0$  line have been multiplied by 0.25 to fit them on the same scale as the HC<sup>18</sup>O<sup>+</sup> line.

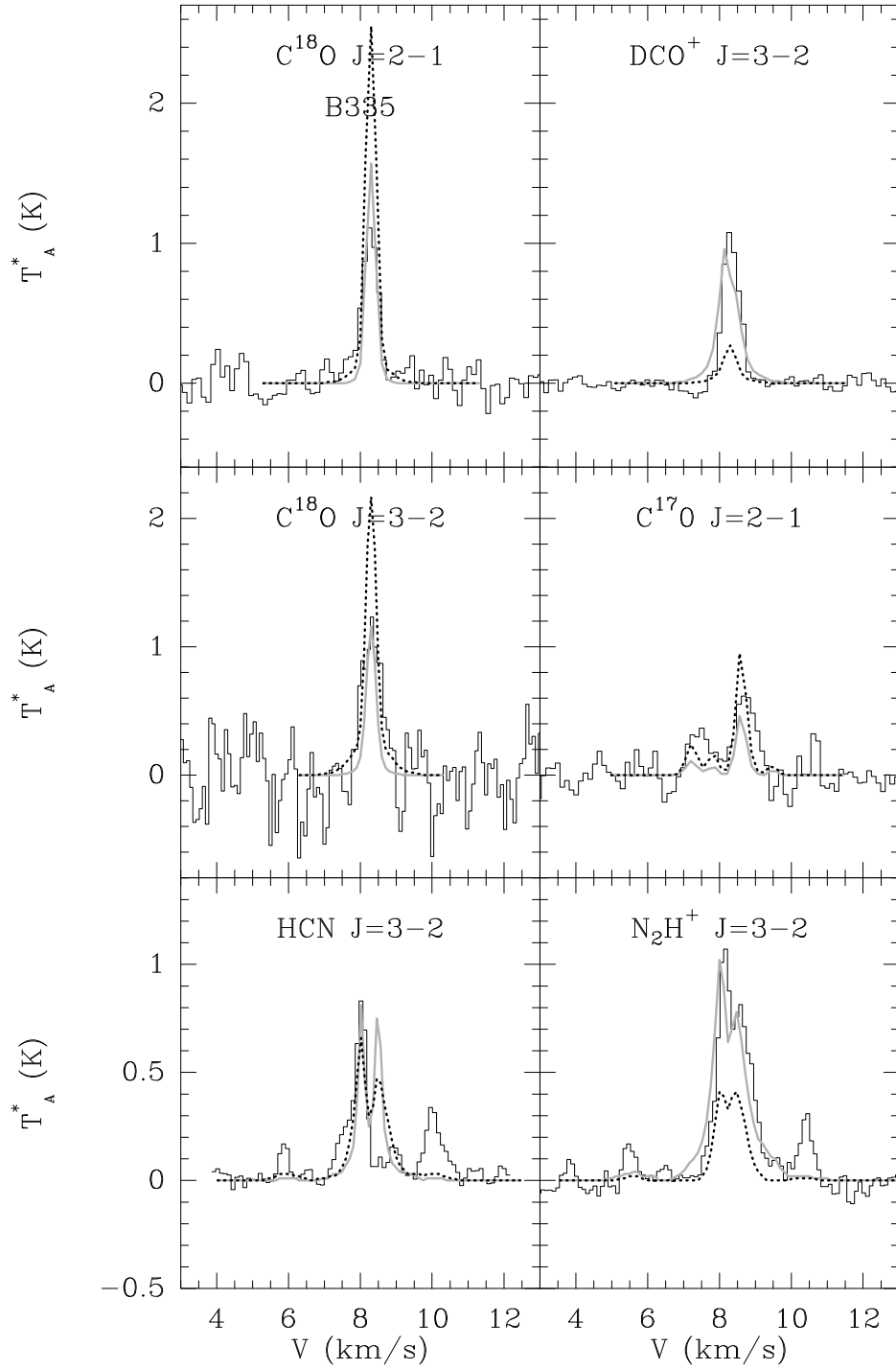


FIG. 5.— Selected observations of isotopes of CO, DCO<sup>+</sup>, HCN, and N<sub>2</sub>H<sup>+</sup> are shown as solid black histograms and the predicted lines from the model are shown as gray solid lines (step functions) dotted lines (chemical abundances).

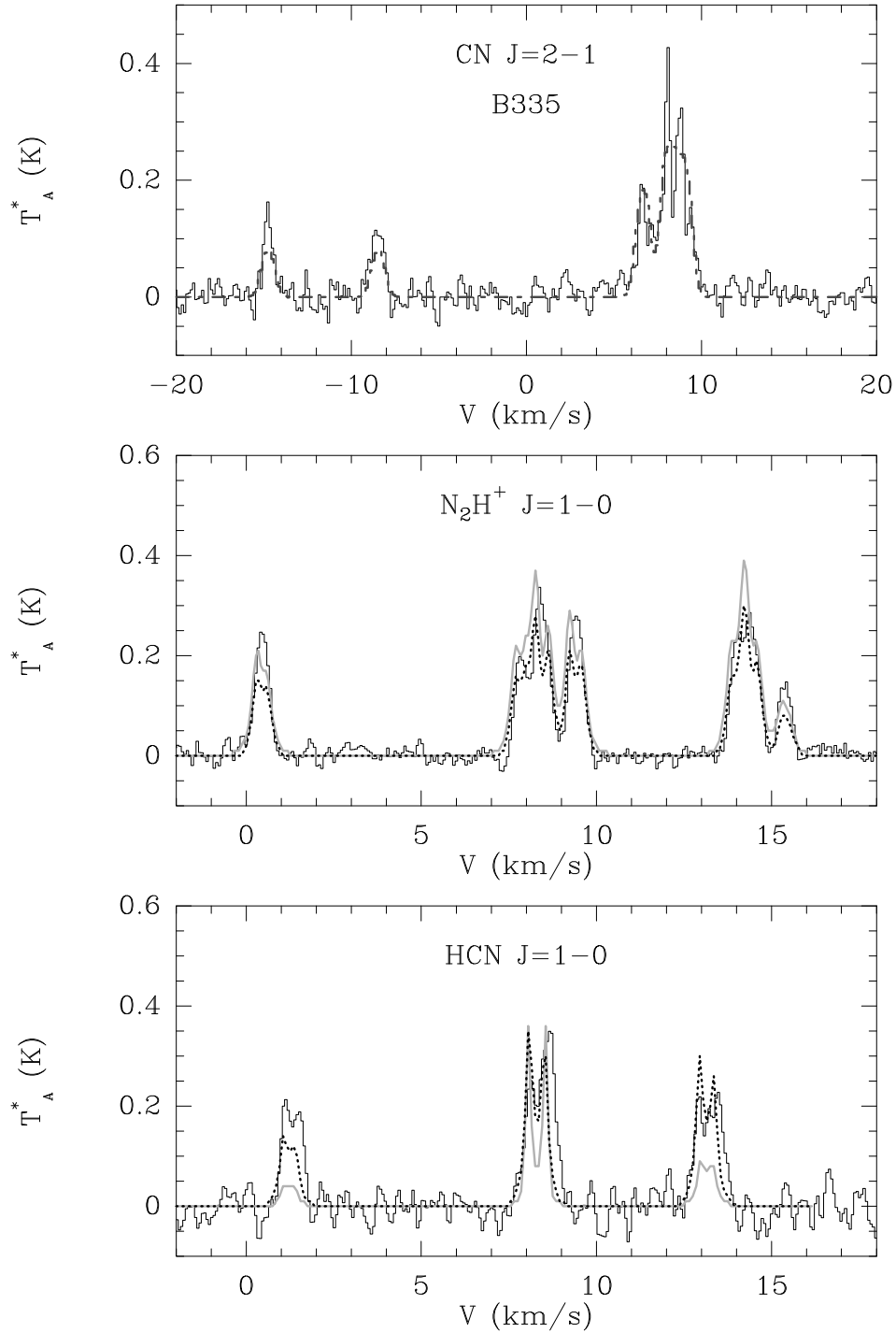


FIG. 6.— The observations of the CN  $J=2 \rightarrow 1$ ,  $N_2H^+ J=1 \rightarrow 0$  and HCN  $J=1 \rightarrow 0$  lines are shown as black solid histograms. For CN, the dotted line is a fit of Gaussians to the hyperfine components, not a true model. The fit to hyperfine components clearly does not reproduce the shape of the main group of lines. The dip is centered at  $8.35 \text{ km s}^{-1}$ , indicating that the main group is self-reversed. For  $N_2H^+$  and HCN  $J=1 \rightarrow 0$ , the gray solid (step functions) and dotted (chemical abundances) lines are predictions of the radiative transfer model.

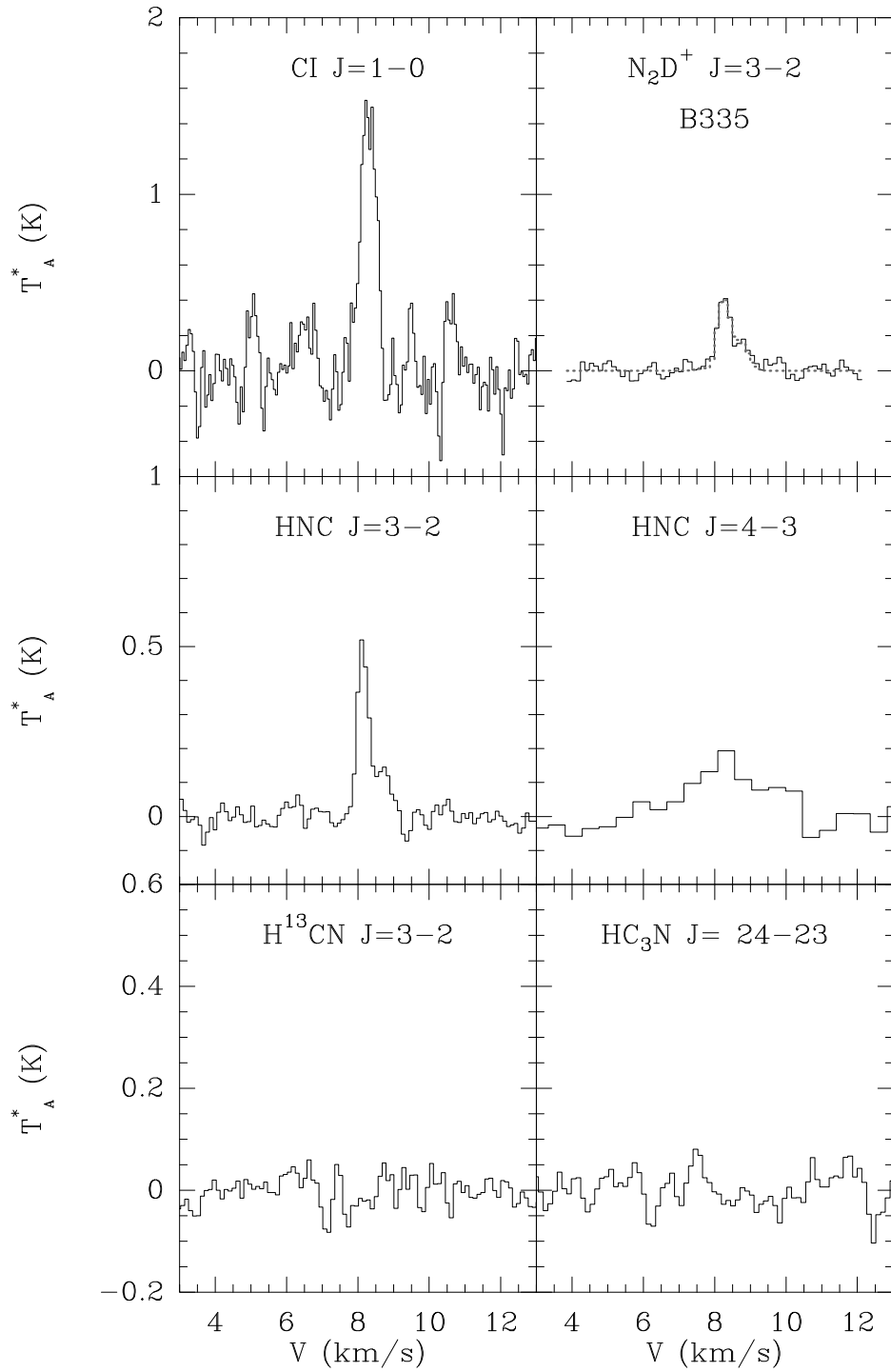


FIG. 7.— The observations of lines that are not modeled in full detail. Some have hyperfine structure. The ones with good fits using hyperfine components show the fit with a dashed line.

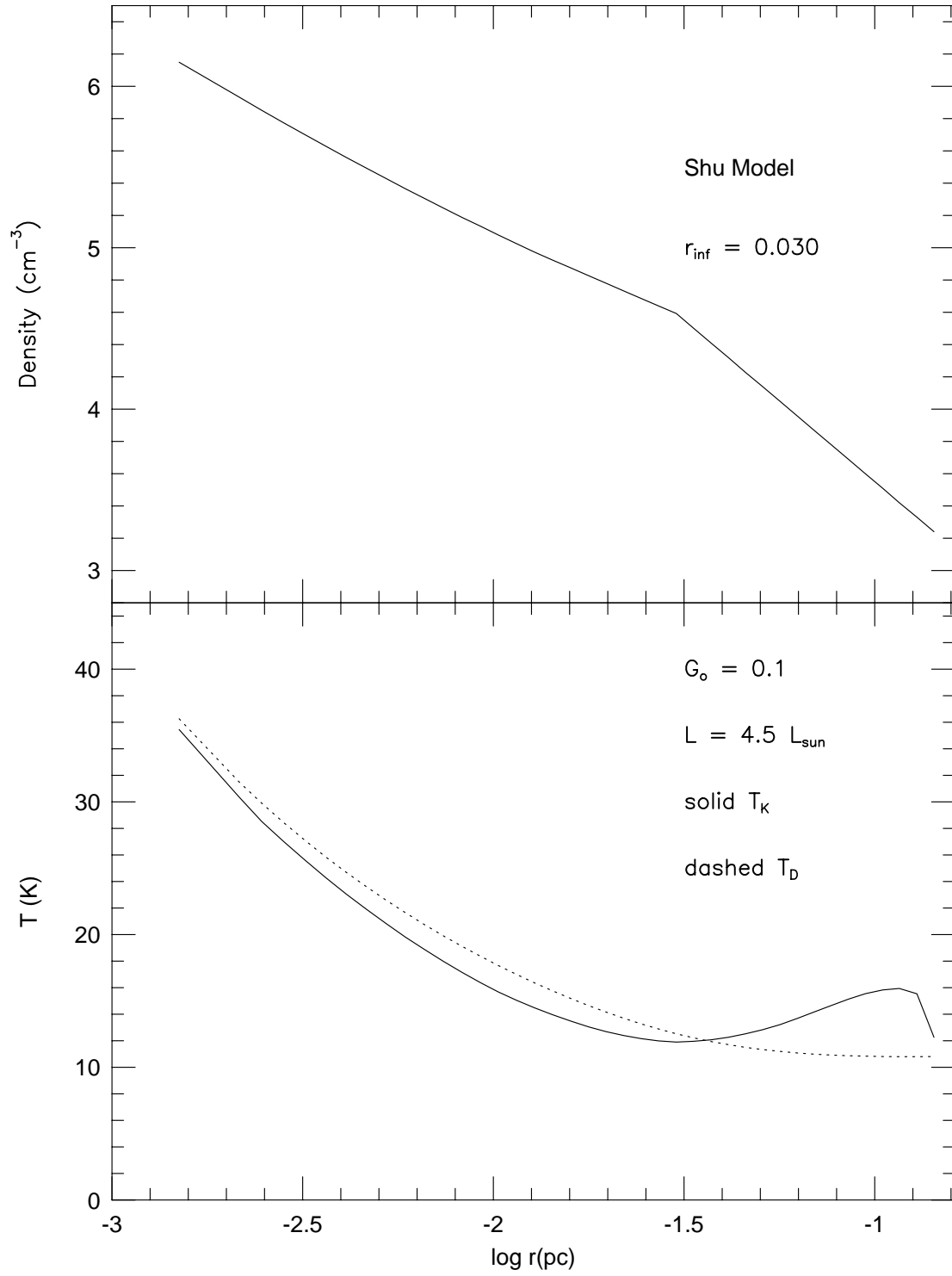


FIG. 8.— The density and temperatures for gas and dust plotted as a function of radius for the standard model.

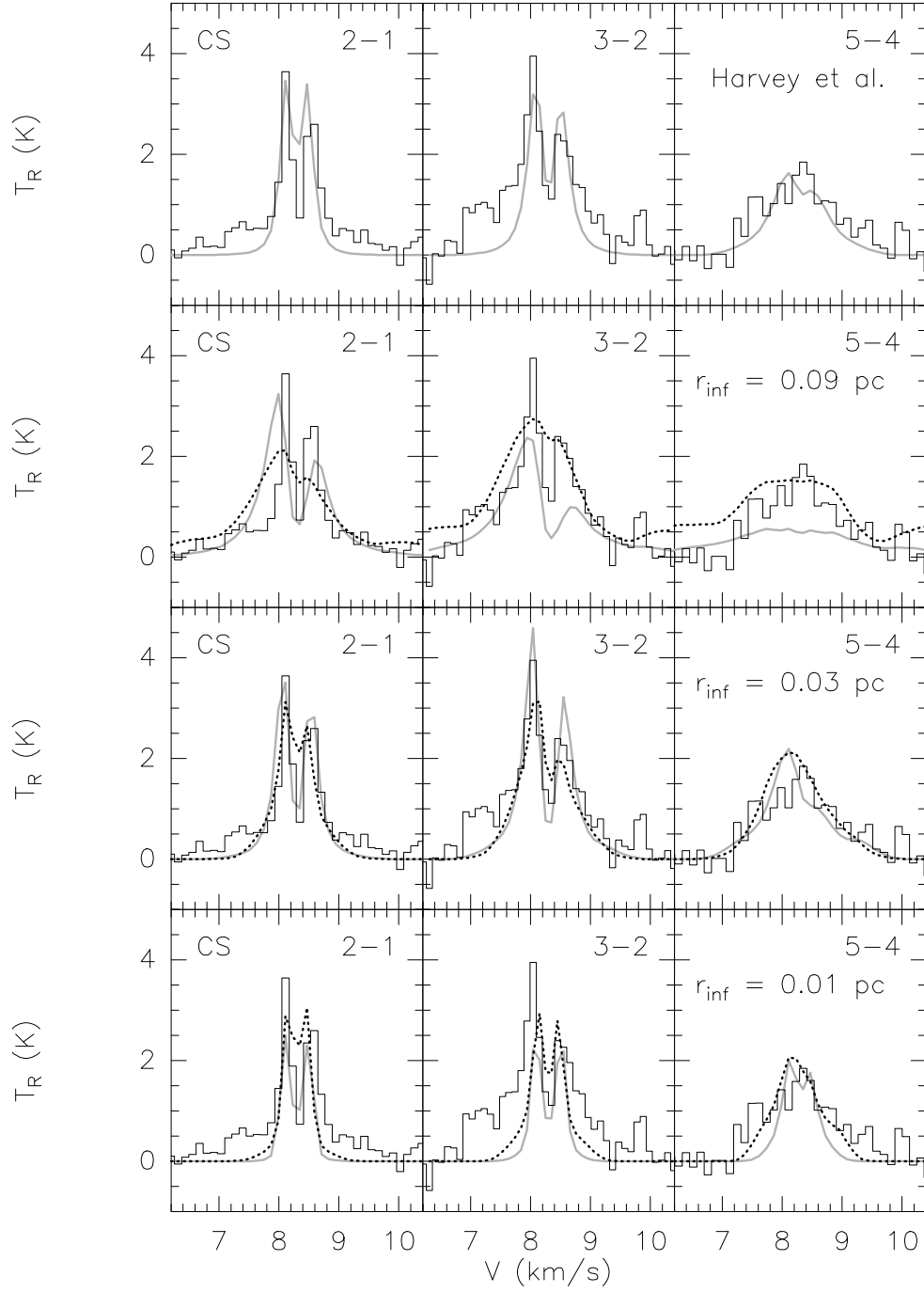


FIG. 9.— The observed CS lines from Zhou et al. (1993) are plotted with the line profiles predicted by various models. The step function models are gray and the evolutionary models are dotted. The bottom panel shows the best model with  $r_{inf} = 0.01$  pc; the second panel from the bottom shows the best model with  $r_{inf} = 0.03$  pc (same as Fig. 1); the third panel from the bottom shows the best model with  $r_{inf} = 0.09$  pc; and the top panel shows the best model with the  $r_{inf} = 0.03$  pc, but with densities enhanced by a factor of 5 everywhere, as favored by Harvey et al. (2001).

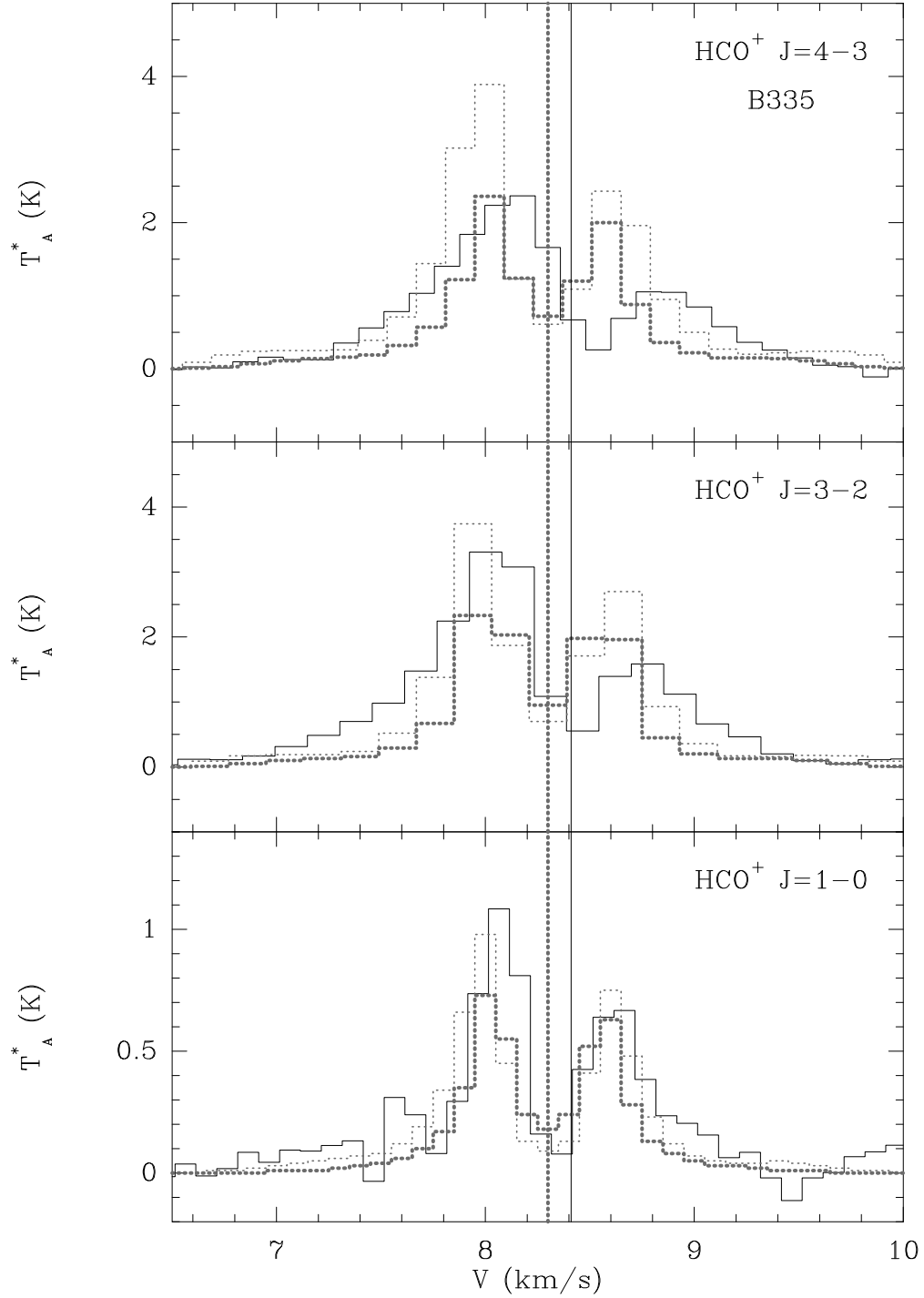


FIG. 10.— The observed HCO<sup>+</sup> lines are plotted on an expanded scale, with the line profiles of the best step function model (dashed) and chemical model (heavy dashed). The solid vertical line is at 8.41 km s<sup>-1</sup>, the average velocity of the dip, while the dotted vertical line is at 8.30 km s<sup>-1</sup>, the mean velocity for optically thin lines. The shift of the dip velocity to higher velocities seen in the observations is not reproduced in the models.

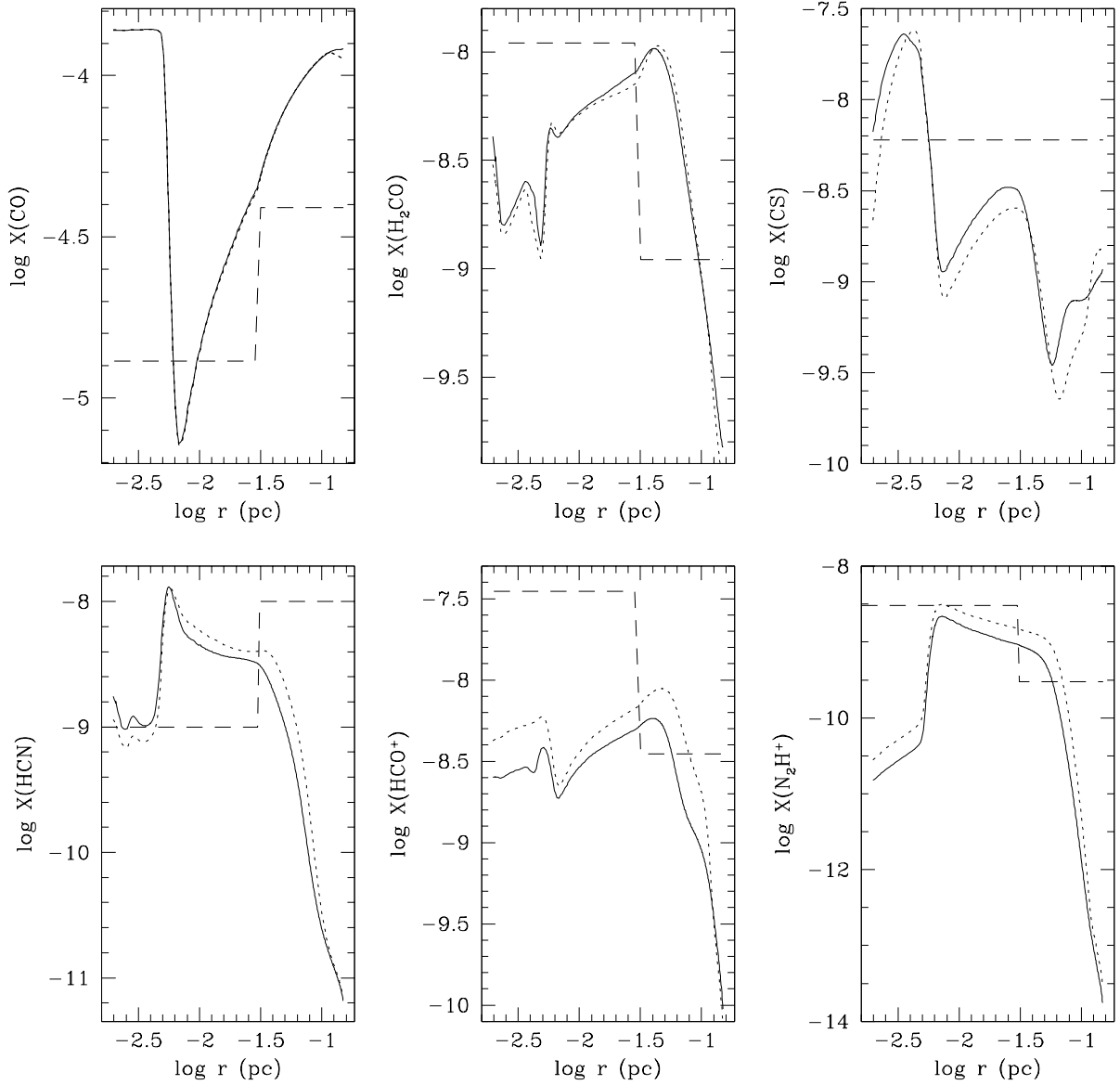


FIG. 11.— Abundance profiles. The dashed line shows the step function abundances, and the solid and dotted lines represent the abundances calculated from the chemical evolution model of Lee et al. (2004) in the time step for  $r_{inf} = 0.03$  pc. In both chemical models, we used the initial sulfur abundance greater than the standard value in Lee et al. (2004) by a factor of 5. In the chemical model with dotted lines, the cosmic-ray ionization rate is two times greater than the standard value to give the best fit to observed line profiles (Model 6 in Table 8). The solid line is Model 5, which uses the standard value for ionization rate.

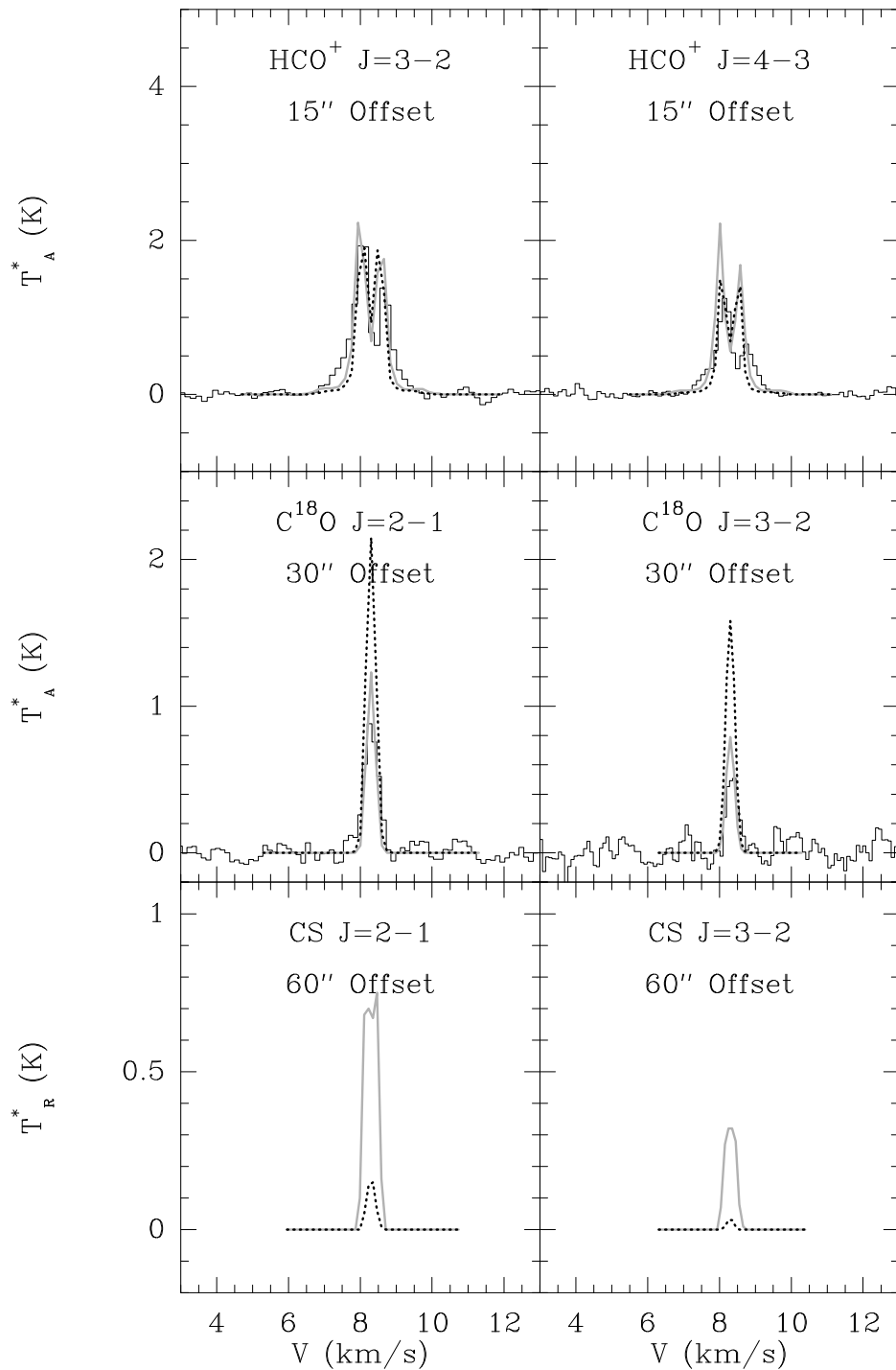


FIG. 12.— Off-center line profiles. The gray solid (step functions) and dotted (chemical abundances) lines are predictions of the radiative transfer model. For  $\text{HCO}^+$  and  $\text{C}^{18}\text{O}$ , we show observed line profiles as histograms. The observations of the CS lines can be seen in Zhou et al. (1993).

TABLE 1  
OBSERVING PARAMETERS

Line	$\nu$ (GHz)	Telescope	$\eta_{mb}$	$\theta_b$ ( $''$ )	$\delta v$ (km s $^{-1}$ )	Ref	Date
CI 1 $\rightarrow$ 0	492.1607	CSO	0.47	16	0.080	1	1996 Jun
CN 2 $\rightarrow$ 1	226.874745	CSO	0.60	27	0.14	1	1998 Jul
C $^{17}$ O 2 $\rightarrow$ 1	224.714368 <sup>a</sup>	CSO	0.81	33	0.17	1	2000 Jun
C $^{18}$ O 2 $\rightarrow$ 1	219.560352	CSO	0.57	28	0.15	1	1998 Jul
C $^{18}$ O 3 $\rightarrow$ 2	329.3305453	CSO	0.82	26	0.10	1	2000 Jul
HCO $^+$ 1 $\rightarrow$ 0	89.188512	Haystack	0.12	25	0.10	1	1994 Jun
H $^{13}$ CO $^+$ 1 $\rightarrow$ 0	86.754330	Haystack	0.12	25	0.10	1	1994 Jun
HCO $^+$ 3 $\rightarrow$ 2	267.557619	CSO	0.65	26	0.18	1	1995 Mar
H $^{13}$ CO $^+$ 3 $\rightarrow$ 2	260.255339	CSO	0.65	26	0.18	1	1995 Mar
HC $^{18}$ O $^+$ 3 $\rightarrow$ 2	255.47940	CSO	0.65	26	0.18	1	1995 Mar
HCO $^+$ 4 $\rightarrow$ 3	356.734288	CSO	0.61	20	0.14	1	1995 Mar
DCO $^+$ 3 $\rightarrow$ 2	216.112604	CSO	0.57	28	0.16	1	1998 Jul
HCN 1 $\rightarrow$ 0	89.635847	TRAO	0.40	61	0.068	2	1997
HCN 3 $\rightarrow$ 2	265.8864343	CSO	0.65	23	0.15	1	1996 Jun
H $^{13}$ CN 3 $\rightarrow$ 2	259.011814	CSO	0.65	23	0.15	1	1996 Jun
HNC 3 $\rightarrow$ 2	271.981142	CSO	0.62	22	0.11	1	1996 Jun
HNC 4 $\rightarrow$ 3	362.630303	CSO	0.53	19	1.62	1	1997 Jul
HC $_3$ N 24 $\rightarrow$ 23	218.324788	CSO	0.56	28	0.18	1	1996 Jun
N $_2$ H $^+$ 1 $\rightarrow$ 0	93.176258 <sup>b</sup>	Haystack	0.12	25	0.10	1	1994 Jun
N $_2$ H $^+$ 3 $\rightarrow$ 2	279.511757 <sup>c</sup>	CSO	0.56	22	0.12	1	1996 Oct
N $_2$ D $^+$ 3 $\rightarrow$ 2	231.321775	CSO	0.73	32	0.21	1	2001 Jul
para-H $_2$ $^{13}$ CO 1 $_{01}$ - 0 $_{00}$	71.02478	NRAO	0.95	89	0.206	3	
H $_2$ $^{13}$ CO 2 $_{12}$ - 1 $_{11}$	137.44996	NRAO	0.72	42	0.1065	3	
H $_2$ CO 2 $_{12}$ - 1 $_{11}$	140.839518	IRAM	0.68	17	0.083	4	
para-H $_2$ $^{13}$ CO 2 $_{02}$ - 1 $_{01}$	141.98375	NRAO	0.72	42	0.103	3	
H $_2$ $^{13}$ CO 2 $_{11}$ - 1 $_{10}$	146.63569	NRAO	0.72	42	0.0998	3	
H $_2$ CO 3 $_{12}$ - 2 $_{11}$	225.697772	IRAM	0.50	12	0.066	4	
H $_2$ CO 3 $_{12}$ - 2 $_{11}$	225.697787	CSO	0.65	27	0.127	1	1996 Jun
para-H $_2$ CO 3 $_{03}$ - 2 $_{02}$	218.222186	CSO	0.65	28	0.131	1	1996 Jun
H $_2$ CO 5 $_{15}$ - 4 $_{14}$	351.768645	CSO	0.53	20	0.083	1	1997 Jun
para-H $_2$ CO 5 $_{05}$ - 4 $_{04}$	362.3530480	CSO	0.53	19	0.085	1	1997 Jun
para-H $_2$ CO 5 $_{23}$ - 4 $_{22}$	365.3634280	CSO	0.53	19	0.085	1	1997 Jun

Note. — (a) Reference frequency for the hyperfine shifts in Ladd et al. (1998); (b) For the isolated hyperfine component (Lee et al. 2001); (c) Reference frequency for the hyperfine shifts in Caselli et al. (2002); (1) This paper; (2) Park et al. 1999; (3) Minh et al. 1995; (4) Zhou et al. 1993.

TABLE 2  
OBSERVATIONAL RESULTS

Molecule	Line	$\int T_A^* dv$ (K km s <sup>-1</sup> )	$T_A^*$ (K)	$v_{LSR}$ (km s <sup>-1</sup> )	$\Delta v$ (km s <sup>-1</sup> )
CI	$J = 1 \rightarrow 0$	0.80(0.04)	1.51(0.18)	8.29(0.01)	0.50(0.03)
CN <sup>b,c</sup>	$J = 2 \rightarrow 1$	0.90(0.02)	0.43(0.02)	8.35(0.04)	0.62(0.07)
C <sup>17</sup> O <sup>a</sup>	$J = 2 \rightarrow 1$	0.46(0.07)	0.57(0.07)	8.39(0.02)	0.49(0.07)
C <sup>18</sup> O	$J = 2 \rightarrow 1$	0.63(0.42)	1.10(0.10)	8.27(0.02)	0.57(0.04)
C <sup>18</sup> O	$J = 3 \rightarrow 2$	0.78(0.09)	2.15(0.26)	8.33(0.04)	0.64(0.08)
HCO <sup>+b</sup>	$J = 1 \rightarrow 0$	0.71(0.05)	1.15(0.11)	8.35(0.03)	0.61(0.10)
H <sup>13</sup> CO <sup>+</sup>	$J = 1 \rightarrow 0$	0.24(0.06)	0.33(0.02)	8.23(0.04)	0.58(0.03)
HCO <sup>+b</sup>	$J = 3 \rightarrow 2$	3.13(0.05)	3.32(0.08)	8.46(0.04)	0.94(0.16)
H <sup>13</sup> CO <sup>+</sup>	$J = 3 \rightarrow 2$	0.46(0.01)	0.76(0.03)	8.25(0.01)	0.57(0.02)
HC <sup>18</sup> O <sup>+</sup>	$J = 3 \rightarrow 2$	0.05(0.01)	0.09(0.01)	8.26(0.04)	0.58(0.10)
HCO <sup>+b</sup>	$J = 4 \rightarrow 3$	2.27(0.15)	2.35(0.06)	8.55(0.03)	0.97(0.12)
DCO <sup>+</sup>	$J = 3 \rightarrow 2$	0.78(0.03)	1.32(0.04)	8.35(0.01)	0.55(0.02)
HCN <sup>b,c</sup>	$J = 1 \rightarrow 0$	0.59(0.10)	0.35(0.05)	8.39(0.01)	0.70(0.10)
HCN <sup>b</sup>	$J = 3 \rightarrow 2$	0.81(0.03)	0.80(0.02)	8.40(0.20)	1.01(0.04)
H <sup>13</sup> CN	$J = 3 \rightarrow 2$	...	< 0.1	...	...
HNC	$J = 3 \rightarrow 2$	0.22(0.01)	0.49(0.03)	8.16(0.01)	0.42(0.03)
HNC	$J = 4 \rightarrow 3$	0.39(0.05)	0.16(0.03)	8.33(0.16)	2.3(0.4)
HC <sub>3</sub> N	$J = 24 \rightarrow 23$	...	< 0.08	...	...
N <sub>2</sub> H <sup>+d</sup>	$J = 1 \rightarrow 0$	0.13(0.01)	0.25(0.02)	8.33(0.01)	0.47(0.02)
N <sub>2</sub> H <sup>+b,c</sup>	$J = 3 \rightarrow 2$	0.95(0.08)	1.00(0.04)	8.38(0.03)	0.38(0.04)
N <sub>2</sub> D <sup>+a</sup>	$J = 3 \rightarrow 2$	0.32(0.04)	0.38(0.04)	8.36(0.02)	0.31(0.05)
H <sub>2</sub> CO	$J_{K-1K+1} = 3_{12} \rightarrow 2_{11}$	0.55(0.01)	0.63(0.02)	8.26(0.01)	0.82(0.02)
para-H <sub>2</sub> CO	$J_{K-1K+1} = 3_{03} \rightarrow 2_{02}$	0.45(0.01)	0.59(0.03)	8.28(0.01)	0.71(0.03)
H <sub>2</sub> CO	$J_{K-1K+1} = 5_{15} \rightarrow 4_{14}$	0.49(0.03)	0.57(0.07)	8.30(0.02)	0.80(0.07)
para-H <sub>2</sub> CO	$J_{K-1K+1} = 5_{05} \rightarrow 4_{04}$	0.40(0.06)	0.31(0.11)	8.53(0.08)	1.22(0.23)
para-H <sub>2</sub> CO	$J_{K-1K+1} = 5_{23} \rightarrow 4_{22}$	...	< 0.2	...	...

Note. — (a) Hyperfine structure:  $\int T_A^* dv$  refers to area under all lines;  $T_A^*$  refers to main peak of blended components;  $v_{LSR}$  and  $\Delta v$  are from fit to blended components; (b) Double-peaked:  $\int T_A^* dv$  is for total area under both peaks;  $T_A^*$  refers to strongest peak;  $v_{LSR}$  refers to dip;  $\Delta v$  is integrated intensity divided by peak  $T_A^*$ . (c) Hyperfine structure:  $\int T_A^* dv$  refers to area under all lines;  $\Delta v$  determined from isolated hyperfine component. (d) All entries refer to the isolated hyperfine component.

TABLE 3  
STANDARD PHYSICAL MODEL

Type	$a$ (km s <sup>-1</sup> )	$r_{inf}$ (pc)	$r_{out}$ (pc)	$L$ (L <sub>⊙</sub> )	$A_V$ (mag)	$G_0$	$\zeta$ (s <sup>-1</sup> )	$b$ (km s <sup>-1</sup> )	$n_e$ (cm <sup>-3</sup> )	$X(CO)$
Shu	0.23	0.03	0.15	4.5	1.3	0.1	$3 \times 10^{-17}$	0.12	$1 \times 10^{-3}$	$7.4 \times 10^{-5}$

TABLE 4  
ISOTOPE RATIOS

C/ <sup>13</sup> C	O/ <sup>18</sup> O	<sup>18</sup> O/ <sup>17</sup> O
70	540	3.5

TABLE 5  
AGGREGATED HYPERFINE SHIFTS<sup>a</sup> AND STRENGTHS<sup>b</sup>

C <sup>17</sup> O		HCN		HCN		N <sub>2</sub> H <sup>+</sup>		N <sub>2</sub> H <sup>+</sup>	
$\Delta v$	$r_i$	$\Delta v$	$r_i$	$\Delta v$	$r_i$	$\Delta v$	$r_i$	$\Delta v$	$r_i$
1.157	0.040	4.849	0.333	1.749	0.037	6.936	0.037	2.015	0.017
0.431	0.122	0.000	0.556	0.303	0.200	5.984	0.185	0.669	0.015
0.241	0.571	-7.072	0.111	-0.030	0.725	5.545	0.111	0.416	0.084
-0.526	0.093	...	...	-0.611	0.001	0.956	0.185	0.266	0.094
-0.926	0.016	...	...	-2.348	0.037	0.000	0.259	0.076	0.089
-1.073	0.095	...	...	...	...	-0.611	0.111	-0.073	0.615
-1.203	0.062	...	...	...	...	-8.006	0.111	-0.601	0.010
...	...	...	...	...	...	...	...	-2.644	0.011
...	...	...	...	...	...	...	...	-2.773	0.014

Note. — (a) Shift in km s<sup>-1</sup> relative to the assumed central velocity of 8.30 km s<sup>-1</sup>; (b) Relative strength ( $r_i$ ) normalized so that  $\sum r_i = 1$ .

TABLE 6  
STEP FUNCTION ABUNDANCES

Species	$X(r > r_{inf})$	$X(r < r_{inf})$	AD(Step)	AD(Chem)
CS	$6.0 \times 10^{-9}$	$6.0 \times 10^{-9}$	6.88	6.78
C <sup>18</sup> O	$7.4 \times 10^{-8}$	$2.5 \times 10^{-8}$	3.00	3.22
HCO <sup>+</sup>	$3.5 \times 10^{-9}$	$3.5 \times 10^{-8}$	3.95	4.02
DCO <sup>+</sup>	$6.0 \times 10^{-11}$	$6.0 \times 10^{-10}$	1.87	3.27
N <sub>2</sub> H <sup>+</sup>	$3.0 \times 10^{-10}$	$3.0 \times 10^{-9}$	5.15	6.14
HCN	$1.0 \times 10^{-8}$	$1.0 \times 10^{-9}$	5.43	4.73
H <sub>2</sub> CO	$7.0 \times 10^{-10}$	$7.0 \times 10^{-9}$	2.64	3.22
para-H <sub>2</sub> CO	$4.0 \times 10^{-10}$	$4.0 \times 10^{-9}$	...	...

TABLE 7  
VARIATIONS IN THE PHYSICAL MODEL

$r_{inf}$	Density factor	$\langle AD \rangle^a$	Chem Mod.	$\langle AD \rangle^a$
0.01	1.0	4.62	6	4.93
0.03	1.0	3.75	6	4.15
0.09	1.0	5.38	6	4.95
0.03	5.0	4.02	...	...

<sup>a</sup>The mean value of AD for all species.

TABLE 8  
CHEMICAL MODELS

Model	Type	Dust Surface	$X(S)$	$\zeta$ ( $s^{-1}$ )	$\langle AD \rangle^a$
Model 1	Step	...	...	...	3.75
Model 2	Chem	SiO <sub>2</sub>	$4 \times 10^{-8}$	$3.0 \times 10^{-17}$	5.05
Model 3	Chem	CO	$4 \times 10^{-8}$	$3.0 \times 10^{-17}$	4.84
Model 4	Chem	H <sub>2</sub> O	$4 \times 10^{-8}$	$3.0 \times 10^{-17}$	5.89
Model 5	Chem	SiO <sub>2</sub>	$2 \times 10^{-7}$	$3.0 \times 10^{-17}$	4.25
Model 6	Chem	SiO <sub>2</sub>	$2 \times 10^{-7}$	$6.0 \times 10^{-17}$	4.15
Model 7	Chem	SiO <sub>2</sub>	$2 \times 10^{-7}$	$1.5 \times 10^{-16}$	4.23

<sup>a</sup>The mean value of AD for all species.